Disrupted endosomal trafficking of the Vangl-Celsr polarity complex underlies congenital anomalies in trachea-esophageal morphogenesis

Nicole A. Edwards[1*], Scott A. Rankin[1], Adhish Kashyap[1], Alissa Warren[1], Zachary N. Agricola[1,2], Alan P. Kenny[2], Matthew J. Kofron[1], Yufeng Shen[4,5], Wendy K. Chung[6,7], Aaron M. Zorn[1,3,8*]

[1]Center for Stem Cell and Organoid Medicine (CuSTOM), Perinatal Institute, Division of Developmental Biology, Cincinnati Children's Hospital Medical Center, Cincinnati, OH, 45208 USA

[2]Perinatal Institute, Division of Neonatology, Cincinnati Children's Hospital Medical Center, Cincinnati, OH, 45208 USA

[3]University of Cincinnati, College of Medicine, Cincinnati, OH, USA

[4]Department of Systems Biology, Columbia University Irving Medical Center, New York, NY, 10032 USA

[5]Department of Biomedical Informatics, Columbia University Irving Medical Center, New York, NY, 10032 USA

[6]Department of Pediatrics, Boston Children's Hospital, Harvard Medical School, Boston, MA, 02115 USA

[7]Departments of Pediatrics and Medicine, Columbia University Irving Medical Center, New York, NY

[8]Lead contact

*Correspondence: aaron.zorn@cchmc.org, nicole.edwards@cchmc.org

Summary

Disruptions in foregut morphogenesis can result in life-threatening conditions where the trachea and esophagus fail to separate properly, such as esophageal atresia (EA) and tracheoesophageal fistulas (TEF). The developmental basis of these congenital anomalies is poorly understood, but recent genome sequencing reveals that *de novo* variants in intracellular trafficking genes are enriched in EA/TEF patients. Here, we confirm that mutation of orthologous genes in *Xenopus* disrupts trachea-esophageal separation similar to EA/TEF patients. We show that the Rab11a recycling endosome pathway is required to localize Vangl-Celsr polarity complexes at the luminal cell surface where opposite sides of the foregut tube fuse. Partial loss of endosome trafficking or Vangl-Celsr complexes disrupts epithelial polarity and mutant cells accumulate at the fusion point, fail to downregulate Cadherin, and do not separate into distinct trachea and esophagus. These data provide insights into the mechanisms of congenital anomalies and general paradigms of tissue fusion during organogenesis.

Introduction

Esophageal atresia (EA) and tracheoesophageal fistulas (TEF), which affect approximately 1 in 3000 newborns, are life-threatening congenital anomalies that arise when the embryonic foregut does not separate correctly into distinct trachea and esophageal tubes[1-4]. This results in esophageal discontinuity (EA) and/or a pathological connection between the trachea and esophagus (TEF). Rarer are laryngeal-tracheal-esophageal-clefts where, in some extreme cases, the foregut fails to separate along its entire length, essentially resulting in a complete TEF[5]. Roughly half of EA/TEF patients also have variably penetrant co-occurring anomalies in other organs, including gastrointestinal, pulmonary, cardiovascular, renal, and central nervous system, suggesting undefined syndromes[6,7]. The genetic etiology of tracheoesophageal anomalies is poorly understood and is associated with spontaneous *de novo* nucleotide variants, chromosomal rearrangements, copy number variation and indels in affected newborns[1,8]. Known variants only account for 10-15% of cases worldwide with the remaining having no identified risk gene. Even when the causative variants are known, why they result in tracheoesophageal anomalies is unclear since the cellular mechanisms governing foregut morphogenesis are poorly understood.

Tracheoesophageal morphogenesis begins when the foregut endoderm is patterned along the dorsal-ventral axis by an evolutionarily conserved Hedgehog-Wnt-BMP signaling network, resulting in dorsal Sox2+ esophageal progenitors and ventral Nkx2-1+ respiratory progenitors[9-12]. After patterning, the foregut constricts at the midline, and a population of epithelial cells on either side of the foregut tube that express both dorsal and ventral markers (Sox2/Nkx2-1/Islet1)

62 come together and adhere, forming a transient epithelial bilayer[13,14]. Epithelial cells at the fusion
63 point then progressively lose adhesion to one another and integrate into either the ventral or
64 dorsal foregut as the surrounding Foxf1+ splanchnic mesoderm invades between the nascent
65 trachea and esophagus[14]. Thus, the single foregut epithelial tube fuses, reorganizes its cellular
66 junctions, and then undergoes fission with coordinated cell rearrangements to reconnect the
67 epithelia into two separate tubes. How cell signaling and transcription factors regulate the
68 cellular processes of tracheoesophageal morphogenesis is unclear.
69
70 Similar epithelial fusion and fission events are crucial for the morphogenesis of many tissues,
71 including the heart, oral palate, eyes, inner ear, urogenital sinus, and neural tube; organ
72 systems that can also be disrupted in complex EA/TEF patients, suggesting shared biological
73 mechanisms[15]. Such tissue fusion and fission events involve dynamic and coordinated changes
74 in cell adhesion and polarity[15,16]. For instance, studies of vertebrate neural tube closure and
75 *Drosophila* retina morphogenesis indicate that the precise spatial and temporal coordination of
76 cell adhesion and cell polarity across different epithelial populations is essential for proper tissue
77 fusion. Less is known about how epithelial polarity and adhesion, likely downstream of
78 Hedgehog and BMP signaling[17], are regulated in tissue fission events like urogenital sinus-
79 hindgut separation. A remaining challenge in the field is understanding how the proteins involved
80 in cell adhesion, cell polarity, and cell junctions are orchestrated to regulate epithelial
81 remodeling during morphogenesis[18-21].
82
83 We recently found in *Xenopus* that Rab11+ recycling endosomes somehow regulate
84 tracheoesophageal morphogenesis downstream of Hedgehog signaling[14]. Rab11 is a small
85 GTPase required for the intracellular recycling of endosomal vesicles that cells use to transport
86 newly synthesized proteins from the Golgi to the plasma membrane and to change the
87 composition of specific plasma membrane domains by internalizing receptors and other cell
88 surface proteins[22]. How recycling endosomes regulate epithelial remodeling in the foregut was
89 unknown. However, recent whole-genome sequencing of EA/TEF patients who exhibit complex
90 multi-organ phenotypes revealed an enrichment of potentially damaging *de novo* variants in
91 genes involved in endocytosis and intracellular trafficking[23]. This finding and our previous
92 observations prompted us to test the hypothesis that endosome trafficking represents a critical
93 morphogenetic bottleneck in tracheoesophageal separation and to explore the underlying
94 cellular mechanisms.
95
96 Here we demonstrate that the recycling endosome pathway is required upstream of the

97 Vangl-Celsr cell polarity complex for proper fission of the foregut tube. Mechanistically, Rab11a
98 localizes the transmembrane protein Vangl2 to the midline luminal cell surface where
99 juxtaposing apical sides of the foregut touch, localize Cadherin, and adhere to one another to
100 form the transient epithelial bilayer. Rab11a and Vangl-Celsr complexes at the contact surface
101 appear to confer an "apical memory" essential for maintaining the cellular organization of
102 transient bilayer and its subsequent resolution. A partial loss of 1) core endosome trafficking
103 components, 2) orthologs of EA/TEF patient risk genes, or 3) the Vangl-Celsr proteins disrupt
104 cell polarity and the orientation of cell division in the transient bilayer. Mutant cells accumulate in
105 a disorganized septum, fail to internalize E-cadherin (Cdh1) from the rounding cell surfaces, and
106 the foregut does not separate into trachea and esophagus, resulting in an extended
107 tracheoesophageal fistula. This unexpected Vangl-Celsr activity is distinct from their well-known
108 roles in planar cell polarity (PCP) which orients cells within the plane of the epithelium. Together,
109 these results indicate that failure to maintain localized endosome-mediated epithelial polarity
110 during foregut morphogenesis may be a common disease mechanism underlying EA/TEF in
111 many patients and may have broad implications for tissue fusion-fission events in the
112 morphogenesis of other organs.
113
114 **Results**
115 **Mutation of endosome pathway genes implicated from EA/TEF patients cause TEF in**
116 ***Xenopus***
117 Recent genome sequencing of complex EA/TEF patients revealed a significant enrichment of
118 potentially damaging and missense *de novo* heterozygous variants in genes involved in
119 intracellular trafficking and endocytosis[23]. This was intriguing considering our discovery that the
120 recycling endosome pathway was somehow involved in tracheoesophageal morphogenesis
121 downstream of Hedgehog signaling[14]. A meta-analysis of experimentally validated protein-
122 protein interactions from the STRING database[24] confirmed that many proteins encoded by
123 patient genes interact with core recycling endosome components (Figure 1A).
124
125 To systematically test the role of endosome trafficking in EA/TEF and determine if the patient
126 variants were likely to be causative risk alleles, we mutated orthologous genes in *Xenopus*
127 *tropicalis* using F0 CRISPR-Cas9 gene editing. We compared the resulting phenotypes to those
128 caused by mutations in core endosome pathway genes. We designed guide RNAs (gRNAs) to
129 create indel mutations early in the coding sequence that were predicted to disrupt protein
130 function by creating a premature stop codon or missense mutations leading to nonsense-
131 mediated decay[25,26]. Cas9-gRNA complexes were injected at the one-cell stage, and after three
132

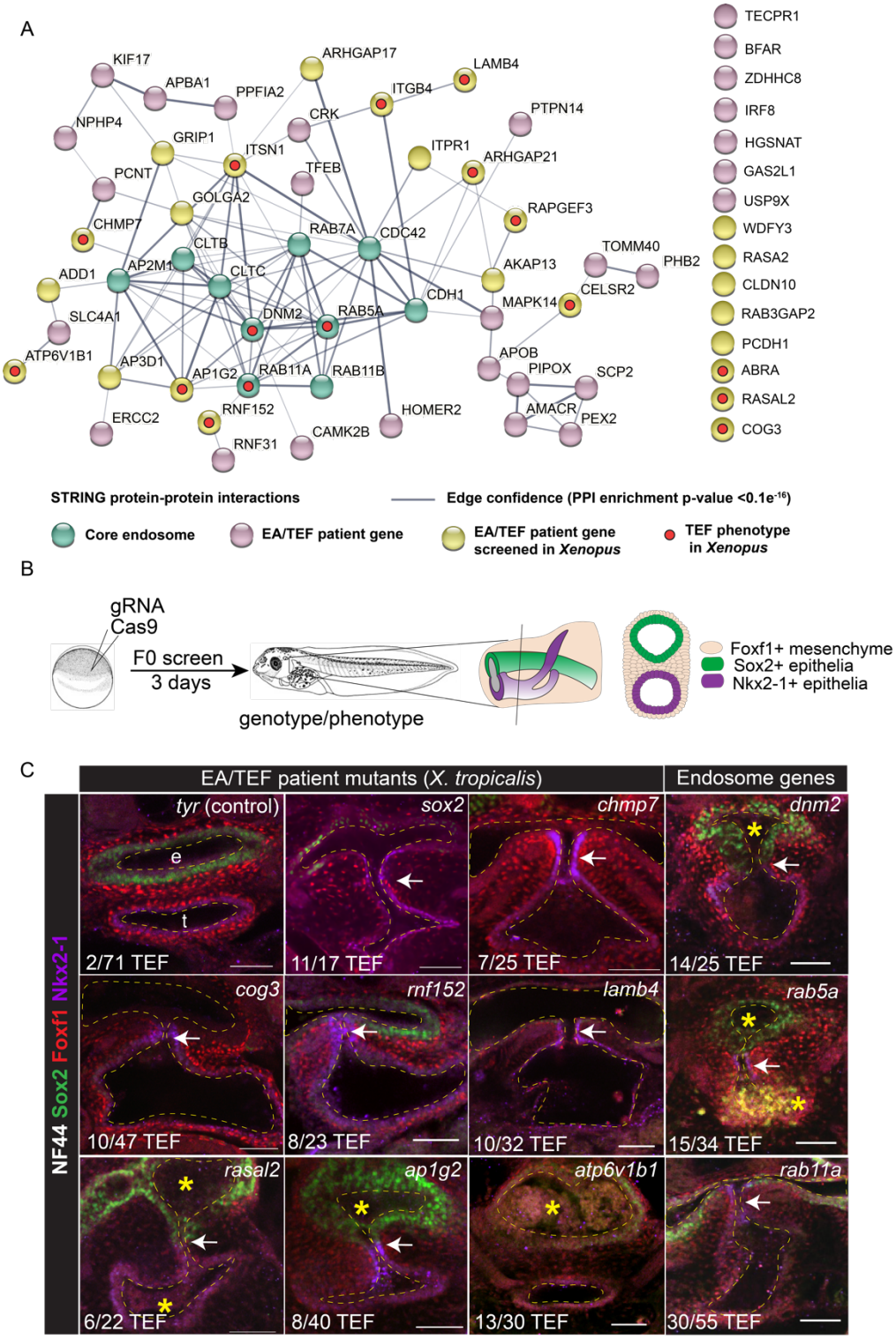

Figure 1. Mutating EA/TEF patient endosome trafficking genes causes TEDs in *Xenopus*. A) STRING Database interactome of endosome-related proteins with potentially pathogenic variants identified in and a curated list of core endosome pathway proteins and putative protein cargo. B) Experimental design of F0 CRISPR-Cas9 *X. tropicalis* mutagenesis screen to validate candidate risk genes. C) Confocal images of CRISPR-Cas9 *X. tropicalis* F0 mutants at NF44 stained for Sox2 (green), Foxf1 (red), and Nkx2-1 (purple). Hashed yellow lines indicate the trachea (t) and esophageal (e) lumens. Arrows indicate TEFs. Asterisks indicate dysmorphic or occluded esophagus or trachea. Numbers indicate the proportion of mutant tadpoles with TEF compared to the total mutants screened. Scale bars are 50 μm.

142 days of development, individual embryos were genotyped, and tracheoesophageal
143 morphogenesis was assayed by immunostaining and confocal microscopy (Figure 1B). Guide
144 RNAs that reproducibly caused EA/TEF-like phenotypes with a significant penetrance compared
145 to controls would support the patient's variant being involved in EA/TEF. In contrast, genes that
146 did not reproducibly cause EA/TEF when mutated in *Xenopus* were likely not disease-causing in
147 EA/TEF patients.
148
149 Confirming the result of 10 genes previously screened[23] as well as testing 15 new genes, we
150 found that mutations in 13 out of 25 orthologs of endosome-related patient risk genes result in
151 significant variably penetrant tracheoesophageal anomalies in *Xenopus* (Figure 1C and Table
152 S1; $p<0.05$). In each case, the foregut was correctly patterned into a ventral Nkx2-1+ tracheal
153 domain and a dorsal Sox2+ esophageal domain with surrounding Foxf1+ mesenchyme, and the
154 foregut underwent initial constriction at the midline. However, in many embryos, the foregut
155 failed to separate into distinct tubes and exhibited a persistent fistula (Figure 1C, arrows). These
156 phenotypes were similar to those caused by mutations in the known EA/TEF risk gene *sox2*[23],
157 and mutations in genes encoding key GTPases in endosome trafficking: *dynamin-2* (*dnm2)*,
158 which regulates endocytosis at the cell surface, *rab5a*, which regulates early endosome vesicle
159 trafficking, and *rab11a*[14] that regulates recycling endosomes (Table S1). Most of the mutants
160 that caused in TEF also exhibited a low penetrance (~20%) of dysmorphic esophagus or
161 trachea ranging from stenosis to a thick multilayered epithelium with multiple or occluded
162 esophageal lumens full of cells (Figure 1C, asterisks; Table S1).
163
164 Genotyping demonstrated an 80% average indel mutation rate (% alleles mutated per embryo)
165 across all gRNAs with a range of 58-90% (Table S1 and Figure S1A). Most gRNAs that
166 reproducibly cause TEF had a mutation burden exceeding 75%. Sequencing analysis revealed
167 that a given gRNA often produced a reproducible pattern of 1-3 different mutations (Figure S1B,
168 source data in Table S2; see STAR methods for details on the genotype-phenotype analysis).
169 Thus, while different cells in an embryo could have different indels, most cells likely had
170 heterozygous or biallelic mutations. In cases when we had effective antibodies (Dnm2, Rab5a,
171 and Rab11a), western blotting of foregut explants showed a dramatic loss of protein, and
172 immunostaining of unilaterally injected embryos demonstrated that most of the cells (>90%) on
173 the injected side had reduced target protein abundance (Figure S1C-D). Together, these data
174 indicate that the F0 CRISPR strategy results in most embryos being more damaged than
175 heterozygous but not complete nulls, with little cellular mosaicism.
176

177 Interestingly, in some mutants, we observed phenotypes in other tissues, including craniofacial,
178 heart, eye, body axis, and gut coiling defects, organ systems that are also disrupted in many
179 EA/TEF patients. However, we found no evidence of a generalized developmental delay based
180 on developmental milestones such as melanocyte pigmentation and tail fin formation. As
181 expected for genes in essential cellular pathways, some embryos with a very high mutation
182 burden (>80%) exhibited gastrulation arrest and lethality before foregut morphogenesis.
183
184 Taken together, these results confirm that endosome trafficking is critical for tracheoesophageal
185 morphogenesis in *Xenopus* and support the likelihood that variants in endosome-related genes
186 may have caused EA/TEF in some patients.
187
188 **Dynamic endosome localization and epithelial remodeling during foregut morphogenesis**
189 To better understand the cellular mechanisms by which endosome trafficking regulates *Xenopus*
190 foregut morphogenesis, we performed a detailed immunostaining analysis of Dnm2, Rab5a, and
191 Rab11a over 24 hours (at room temperature) when the foregut separates into distinct
192 esophageal and tracheal tubes (Figure 2).
193
194 As previously reported in Nasr et al., 2019[14], just before the foregut midline fuses at NF37, the
195 endodermal tube is a typical pseudostratified columnar epithelium, with Cdh1 localized to the
196 basal-lateral cell borders and in adherens junctions. Apical polarity proteins like aPKC and Par3
197 are localized to the luminal cell surface, whilst Laminin (Lama1) lines the basal surface,
198 contacting the surrounding mesoderm (Figure 2A and Figure S2A-C). As the foregut constricts,
199 apical proteins aPKC and Par3 are downregulated at the midline, where the opposing epithelia
200 touch and Tjp1+ tight junctions are lost (Figure 2B and Figure S2D-G). This is coincident with
201 the localization of Cdh1 to the luminal contact surface (Figure 2B, quantification in Figure 2Q),
202 which presumably helps mediate the adhesion of the two sides and the formation of a transient,
203 columnar epithelial bilayer by NF39 (Figure S2J). Throughout this fusion process all foregut
204 epithelial cells (dorsal, ventral, and midline) have Dnm2 detectable at the apical-lateral
205 membrane and subapical Rab5a+ early endosome vesicles (Figure 2C-F, quantification in
206 Figure S2H-I). In contrast, Rab11a+ puncta are detectable at the apical membrane of epithelial
207 cells in the foregut with higher intensity levels in the midline epithelial cells that are coming into
208 contact (Figure G-H, quantification in 2Q).
209
210 Twelve hours later, at NF41-42, cell surface Dnm2 and Rab5a+ puncta were observed
211 throughout the epithelial bilayer, as well as in the trachea and esophageal epithelia and the
212 surrounding mesenchyme (Figure 2K,M). At this point, Rab11a colocalized with Cdh1 at the

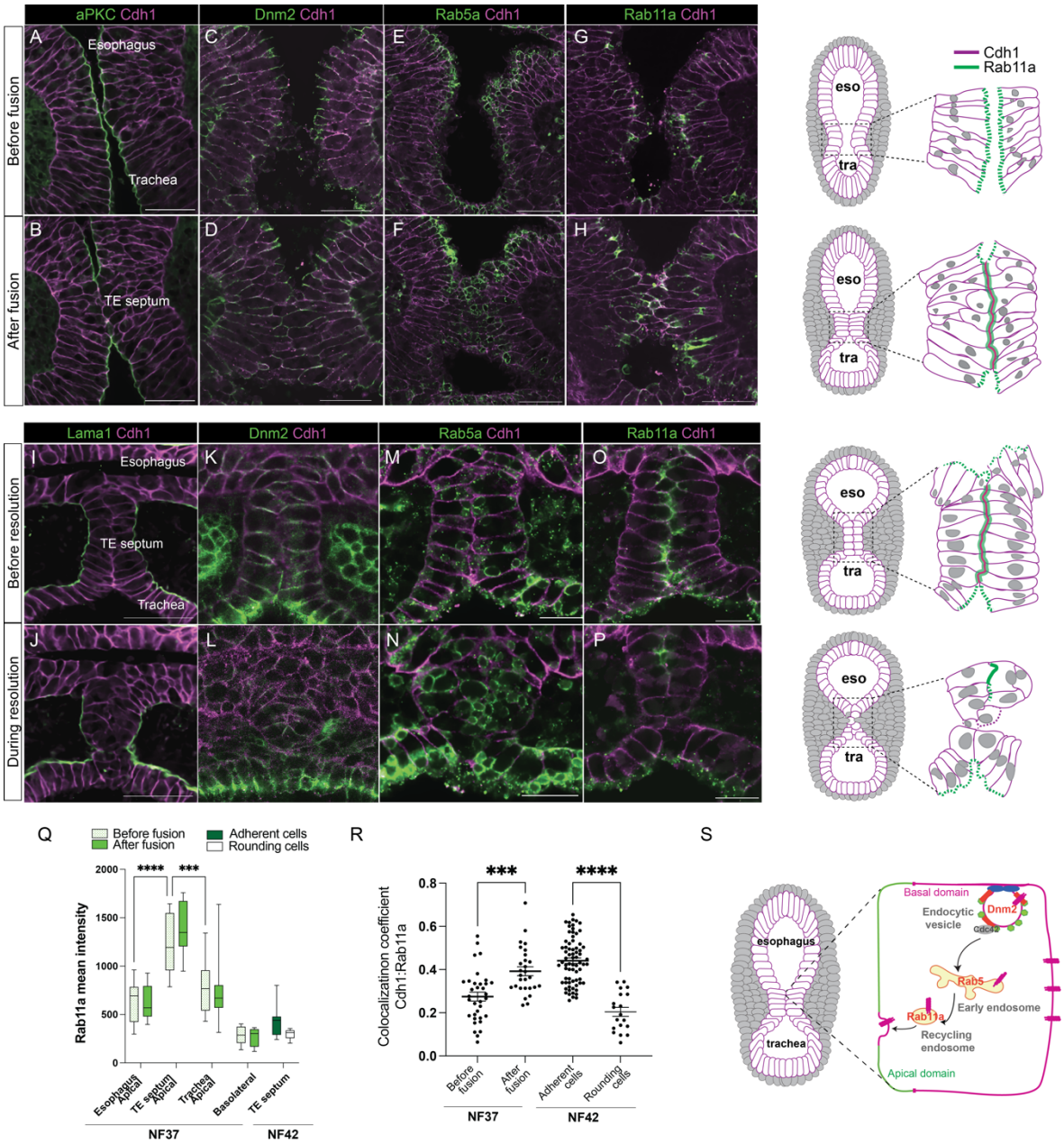

Figure 2. Dynamic endosome localization and epithelial remodeling during tracheoesophageal morphogenesis. A-B, I-J) Immunostaining of aPKC, Laminin (Lama1), and Cdh1 dynamics in the Xenopus foregut during trachea-esophageal morphogenesis. C-H, K-P) Immunostaining of Dnm2, Rab5a, and Rab11a in the Xenopus foregut during trachea-esophageal morphogenesis. Scale bar = 50 μm. Diagrams depict the temporal-spatial dynamics of Cdh1 and Rab11a subcellular localization during tracheoesophageal morphogenesis. Q) Quantification of Rab11a immunostaining intensity during foregut fusion and separation (mean ± min/max, 2W-ANOVA, ****p<0.0001, n=4-6 embryos analyzed). R) Cdh1-Rab11a co-localization at the epithelial interface (Mean Pearson colocalization coefficient ± SEM, *** p<0.001, **** p<0.0001 1W-ANOVA, n=5-13 cells per embryo, N=6-8 embryos per stage). S) A model of how endosome trafficking may mediate Cdh1 re-localization during epithelial fusion.

adhesion surface between the two epithelial sides in the bilayer (Figure 2O-R). As the transient bilayer began to resolve, we observed a downregulation of Rab11a and an increase in large Rab5a+ vesicles in the epithelium, consistent with elevated early endosome activity (Figure

231 2L,N,P). This coincided with a loss of Cdh1 signal on cells rounding up and losing attachment to
232 their neighbors as the mesenchyme invaded to complete separation of the foregut (Figure S2K-
233 L).

234

235 **Asymmetric relocalization of Cdh1 is required for trachea-esophageal separation.**
236 Our results suggested that a localized reduction in Cdh1, possibly mediated by Rab5-dependent
237 endocytic internalization, facilitates foregut separation. To quantitatively assess Cdh1 dynamics
238 and cell-cell contacts, we measured Cdh1 immunostaining intensity normalized to a ubiquitously
239 expressed membrane-GFP transgene in 3D renderings of the contact surfaces between
240 epithelial cells in the bilayer as it was separating. We found that the contact surface area
241 between epithelial cells where the bilayer was separating was significantly smaller, with lower
242 Cdh1 levels, compared to the larger adherent surfaces of the same cells that were still in contact
243 with adjacent esophageal and tracheal epithelium (Figure 3A, B). This suggests that asymmetric
244 relocalization of Cdh1 from the rounding cell surface membrane facilitates the separation of the
245 epithelial bilayer.

246

247 To test whether endocytic removal of Cdh1 from the cell surface was required for resolution of
248 the bilayer, we expressed a Cdh1 mutant (ΔLL-Cdh1) that cannot be internalized by clathrin-
249 dependent endocytosis[27] using *Xenopus* F0 transgenics (Figure 3C). The bipartite transgene
250 *Tg(hhex:trTA;TRE:ΔLL-Cdh1-GFP)* specifically expresses the mutant ΔLL-Cdh1 or a control
251 wildtype (WT)-Cdh1 in the foregut upon administration of doxycycline (DOX). Compared to non-
252 induced and WT-Cdh1 controls, approximately 70% of ΔLL-Cdh1 DOX treated transgenic
253 embryos exhibited a TEF, with a significantly longer segment of unseparated epithelial bilayer
254 (Fig 3D,E). This demonstrates that endocytosis of Cdh1 is required for epithelial bilayer to
255 undergo fission and separate the trachea and esophagus.

256

257 **Endosome trafficking is required for maintenance and resolution of the epithelial bilayer**
258 **during tracheoesophageal morphogenesis**
259 Next, we determined which epithelial remodeling events driving tracheoesophageal
260 morphogenesis require endosome trafficking. Surprisingly, initial foregut constriction and
261 epithelial fusion, with downregulation of aPKC and increased localization of Cdh1 at the contact
262 surface, occurred normally in *dnm2*, *rab5a*, and *rab11a* mutant embryos (Figure 4A). The earliest
263 cellular phenotype we observed was a disorganized septum 4-6 cells wide, with cells in the
264 middle being round rather than the stereotypical columnar epithelial bilayer at NF41 (Figure 4B,

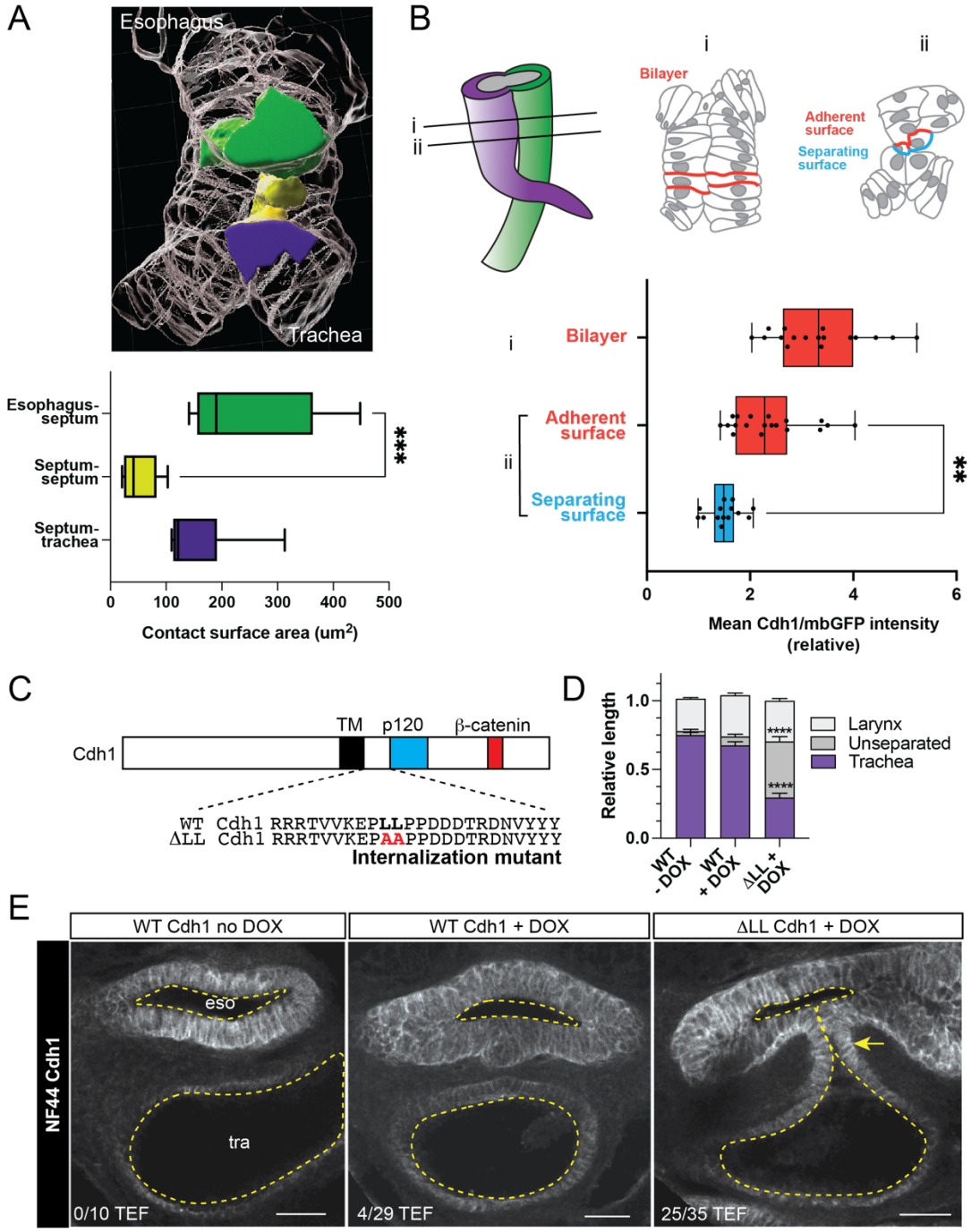

Figure 3. Endocytosis of Cdh1 is required for trachea-esophageal separation. A) 3D cell-surface rendering of the resolving septum; esophageal cells (green), septum cells (yellow), tracheal cells (purple). Septum cells significantly decrease surface contact area with each other compared to the contact between tracheal and esophageal cells (mean ± min/max, *** $p<0.001$ 1W-ANOVA, n=6 cells per embryo, N=9 embryos). B) Diagrams of the separating foregut at i) the intact bilayer and ii) at the point where the bilayer is separating. The graph quantifies Cdh1/mbGFP intensity at cell surfaces in the bilayer, and the adherent versus separating side of the cells are losing contact (mean ± min/max, ** $p<0.01$ 1W-ANOVA, n=5 cells per embryo, N=6 embryos). C) Structure of wild-type (WT) and the ΔLL → AA Cdh1 mutant that cannot be internalized by endocytosis[27]. D) Quantification of the TEF phenotype in ΔLL-Cdh1 mutants compared to WT-Cdh1 and no DOX control embryos (mean ± SEM, ****$p<0.0001$ 1W-ANOVA, n=10-35 embryos, N=3 transgenesis experiments). E) Cdh1 immunostaining and confocal microscopy of NF44 transgenic embryos and controls. Scale bars = 50 μm.

278 quantified in Figure 4E). Moreover, at NF42, when the septum in control embryos is separating,
279 the mutant septum did not downregulate Cdh1 and resolve into the distinct trachea and
280 esophageal tubes. Rather, a disorganized epithelial mass persisted, resulting in a blind-ended
281 fistula (Figure 4C-D, Table S1). We frequently observed blisters in the mutant septa at NF42.
282 Interestingly, the blisters exhibited asymmetric reductions in Cdh1 on the luminal surface,
283 suggesting that some cells in the tissue try to separate from one another, but other cell-cell
284 contacts prevent complete septation (Figure 4D). These results indicate that endosome
285 trafficking is required to maintain an organized epithelial bilayer and suggest that the
286 accumulation of too many cells with persistent Cdh1 at epithelial-epithelial interfaces disrupts
287 the resolution into distinct trachea and esophageal tubes.
288
289 To determine if the accumulation of cells was due to elevated cell proliferation, we quantified
290 confocal Z-stacks of the entire foregut region. We found that neither the total number of cells in
291 the trachea-esophageal septum nor the rate of proliferation (as measured by phosphorylated
292 histone H3 staining) was significantly increased in endosomal mutants compared to controls
293 (Figure 4F-G). Three-dimensional reconstructions demonstrated that the mutant septa were
294 wider (x-axis) and shorter in the rostral-caudal axis (z-axis) compared to controls but were
295 similar in the dorsal-ventral axis (y-axis) (Figure S4). This indicates that mutant cells somehow
296 accumulate across the width of the epithelia septum at the expense of fewer cells along the
297 rostral-caudal extension of the separating trachea and esophagus.
298
299 **Endosome trafficking controls cell polarity and orientation of division in the epithelial**
300 **bilayer**
301 The earliest cellular phenotype we observed in endosome CRISPR mutants was the significant
302 accumulation of cells inside the epithelial bilayer after foregut fusion. Since cells in
303 pseudostratified and columnar epithelia are known to divide into the plane of the tissue to
304 maintain appropriate organization, we considered the possibility that in mutant embryos, cells
305 might aberrantly divide into the middle of the septum and be unable to reintegrate back into the
306 epithelial bilayer contributing to the cell build-up (Figure 5A). To assess the plane of cell division,
307 we measured the angle of the mitotic spindle relative to the basal membrane in the septum of
308 endosomal mutants and controls. While cells in the epithelial bilayer of control embryos divided
309 into the plane of the epithelia as expected, with an average spindle orientation of 0-15°, *dnm2*,
310 *rab5a,* and *rab11a* mutants exhibited a more random distribution of mitotic spindle angles
311 (Figure 5B,C). This defect was primarily localized to the septum, as the mitotic spindle angles in
312 the trachea and esophagus were not significantly different between mutants and controls
313

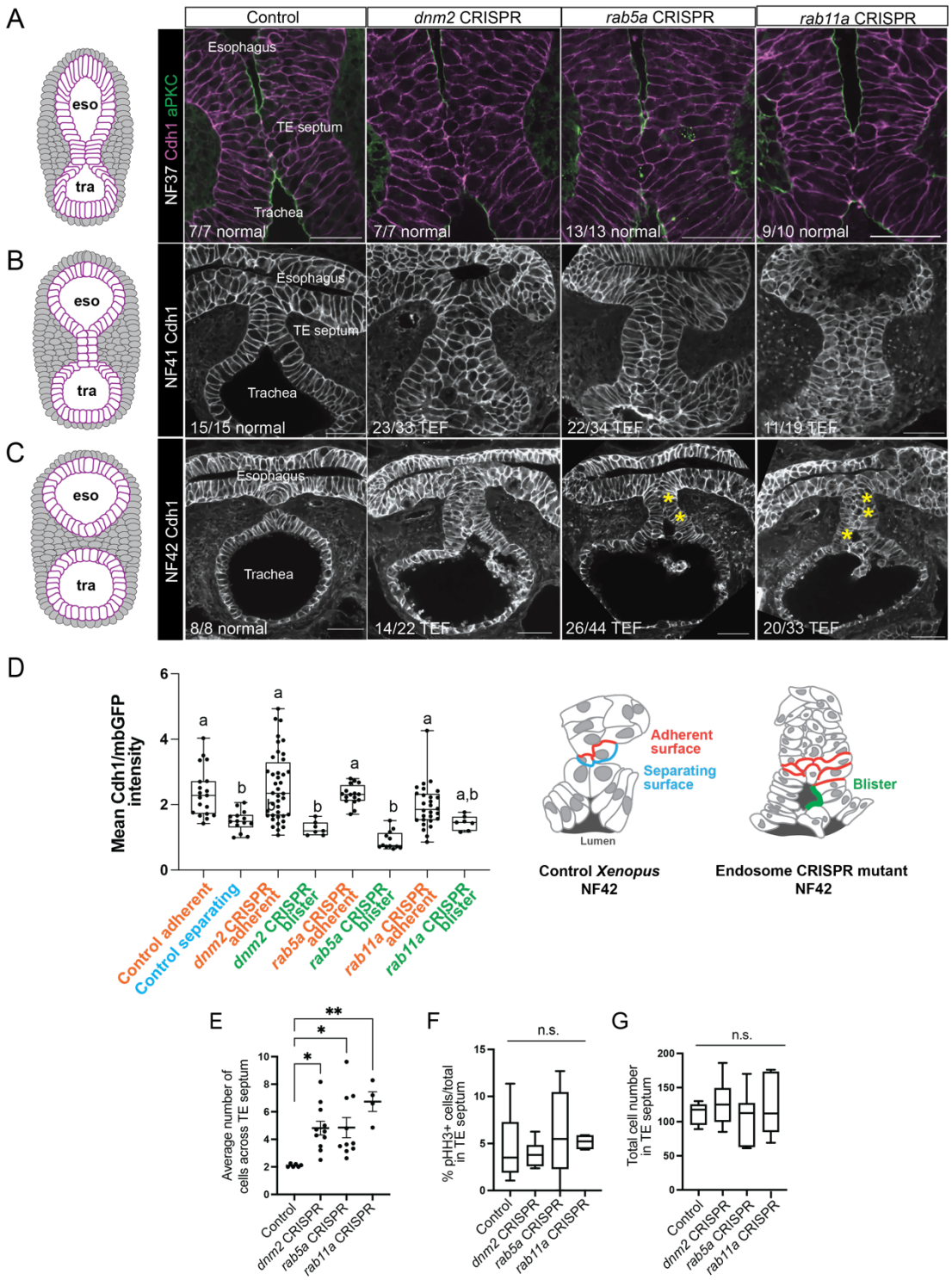

Figure 4. Endosome trafficking is required for resolution of the epithelial bilayer. A) At NF37, the septum in *dnm2*, *rab5a*, and *rab11a* CRISPR mutants undergoes epithelial fusion similar to controls. B) At NF41 the epithelial bilayer in endosome mutants is disorganized compared to controls. C) *dnm2*, *rab5a*, and *rab11a* CRISPR mutants exhibit TEF and blisters in the TE septum (asterisks). Scale bars are 50 µm. D) Quantification of Cdh1/mbGFP intensity in the adherent, separating, and luminal cell surfaces, in control septum, and endosome mutant blisters (mean ± min/max, 1W-ANOVA, different letters indicate $p<0.05$ between groups, n=7-40 cells, N=3-5 embryos) E) The NF41 mutant septa have more cells across the width compared to controls (mean ± SEM, * $p<0.05$ 1W-ANOVA, ** $p<0.01$, N=6-11 embryos). F) There are no significant (n. s.) differences in proliferation (pHH3+/total) or G) total cells in the septum of mutant embryos compared to controls (mean ± min/max, 1W-ANOVA, n=46 embryos).

325 (Figure S4). Thus, loss of endosomal trafficking causes aberrant cell division into the center of
326 the epithelial bilayer, and possibly a defect in epithelial reintegration into the tissue after cell
327 division due to altered apical-basal cell polarity.
328
329 To test whether apical-basal cell polarity was disrupted, we performed immunostaining for
330 laminin, which is secreted from the basal side of epithelia into the extracellular matrix. Indeed,
331 mutant embryos exhibited ectopic laminin deposition in the center of the disorganized septum
332 surrounding the round central cells and in the lumens of blisters within the tissue (Figure 5D-G).
333 These observations are consistent with disrupted endosome trafficking leading to loss of apical-
334 basal polarity in the transient epithelial bilayer, randomized cell division, and cells accumulating
335 in the mutant tracheoesophageal septum.
336
337 **Endosome trafficking localizes Vangl2 to maintain apical memory in the epithelial bilayer**
338 During foregut morphogenesis, when the apical epithelial cell surfaces from either side touch
339 one another, they lose apical markers (aPKC, Par3) and gain Cdh1 (typically basal-lateral) as
340 they adhere and form the transient bilayer. Despite this apparent loss of apical identity, the cells
341 must somehow retain some apical-basal cues to maintain an organized bilayer and undergo cell
342 division in the plane of the epithelium – a process that we found requires endosome trafficking.
343 One candidate pathway that might regulate this process is the Vangl-Celsr polarity complex. In
344 addition to their well-known role in the Wnt/PCP pathway where heterotypic cell-cell interactions
345 between transmembrane Vangl, Celsr, and Frizzled proteins govern cell orientation in the plane
346 of the epithelia[28], Vangl and Celsr are also involved in specifying apical-basal polarity in epithelia
347 by recruiting apical Par3 and aPKC whilst restricting Scrib to the basolateral domain[18,29,30].
348 Furthermore, apical Vangl-Celsr complexes are reported to be internalized by endosomes
349 during polarized cell divisions of the fetal mouse epidermis[31], suggesting a potential mechanistic
350 link in the foregut.
351
352 To assess whether Vangl-Celsr complexes are involved in endosome-dependent epithelial
353 remodeling in the foregut, we performed Vangl2 and Celsr1 immunostaining in combination with
354 Rab11a (antibodies are not available for *Xenopus* Celsr2 and Vangl1). Before foregut fusion,
355 diffuse Vangl2 was observed throughout the foregut epithelia with no apparent difference
356 between apical and basolateral cell domains (Figure 6A,F). However, as the midline epithelia
357 touched, Vangl2 became progressively co-localized with Rab11a puncta at the luminal/apical
358 contact point and subsequent adherent interface of the bilayer (Figure 6, Figure S6). Super-
359 resolution microscopy demonstrated that approximately 40% of Rab11a and Vangl2 puncta at
360

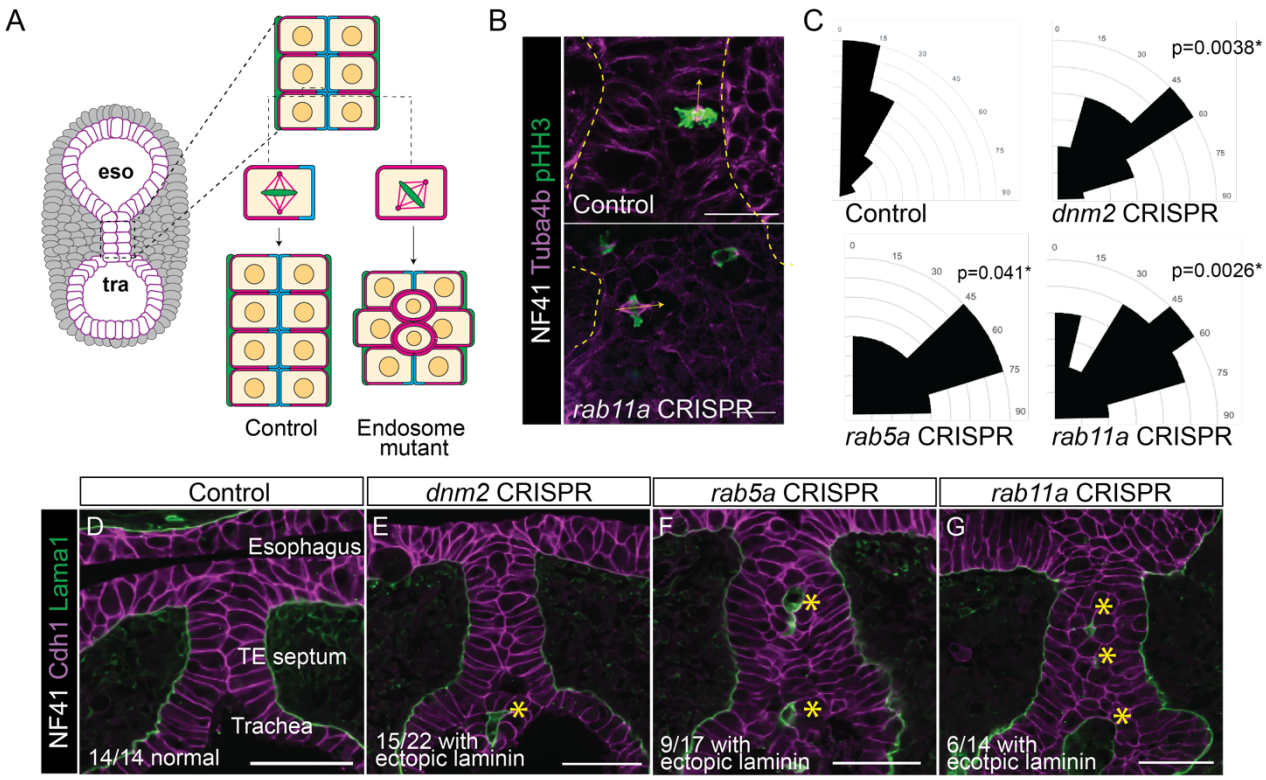

Figure 5. Endosome trafficking controls the polarity of epithelial cell division. A) A model of altered cell division orientation in endosome mutants causing cells to accumulate in the epithelial septum. B) Immunostaining of the mitotic spindle (Tuba4a and phospho-histone H3) was using to measure the angle of cell division at NF41. C) Distribution of mitotic spindle angles is random in endosome mutant epithelial cells compared to controls, which consistently divide between 0-15° (n=3-15 spindles per embryo, Kolmogorov-Smirnov test, N=4-6 embryos. D-G) Endosome mutants have ectopic Laminin deposits (asterisks) inside the blistered disorganized epithelia. Scale bars are 50 µm.

the adherent interface of the bilayer were within 500 nM of each other, consistent with the size of a recycling endosome vesicle[32,33]. In contrast to this dynamic Vangl2 subcellular localization, Celsr1 remained around the entire juxta-membrane region of the epithelial bilayer cells throughout tracheoesophageal morphogenesis (Figure S6E-H).

Considering that endosomes are reported to internalize cell surface Vangl2 in the fetal mouse epidermis[26], this suggested that Vangl2 might be a cargo of the Rab11+ recycling endosomes, transporting it to the cell surface where the epithelia fuse. To test this possibility, we examined Vangl2 localization in the endosome mutants. Vangl2-Rab11a co-localization at the epithelia contact was lost in the disorganized multilayer septum of *dnm2*, *rab5a* and *rab11a* mutants (Figure 6J-N, Figure S6D). However, Celsr1 localization and apical Vangl2 in the esophagus and trachea were unaffected (Figure 6K-M, asterisks, Figure S6I-M), indicating that recycling endosomes are required to localize Vangl2 at the midline apical interface.

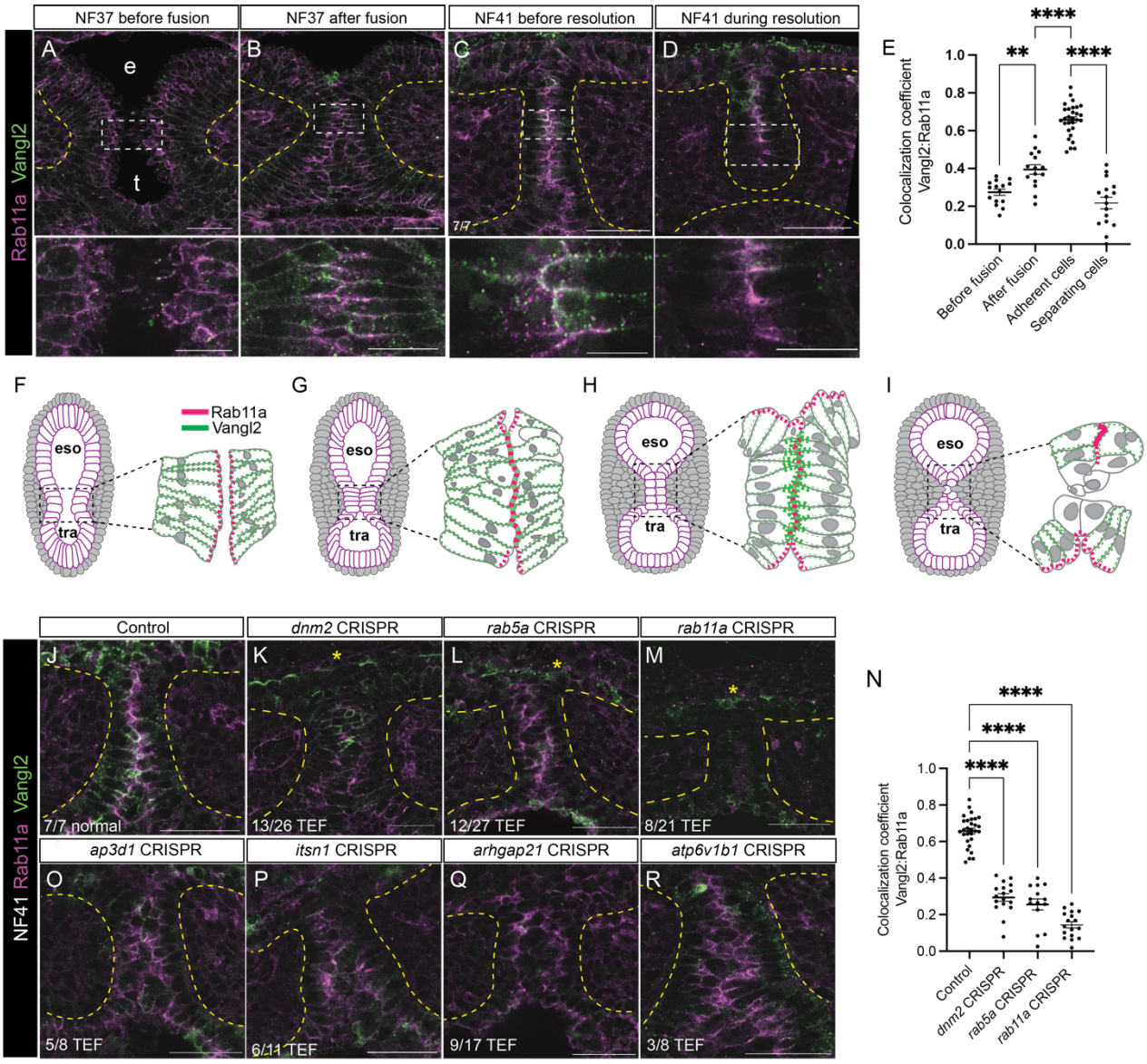

Figure 6. Recycling endosomes localize Vangl2 to maintain apical memory in the transient trachea-esophageal septum. A-D) Time course of Vangl2-Rab11a immunostaining during *Xenopus* tracheoesophageal separation. E) Dynamic Vangl2-Rab11a co-localization at the epithelial interface (Mean Pearson colocalization coefficient ± SEM, *** p<0.001, **** p<0.0001 1W-ANOVA, n=6 cells per embryo, N=5 embryos per stage). F-I) Diagrams of Vangl2-Rab11a localization during foregut separation. J-M) Vangl2 is mis-localized in septum epithelial cells of endosome mutants. N) Endosome mutant septa have significantly lower Vangl2-Rab11a colocalization relative to controls (mean ± SEM, **** p <0.0001 1W-ANOVA, n=5 cells per embryo, N=4-6 embryos per condition). O-R) CRISPR F0 mutation of patient variant orthologous genes in *Xenopus* (*ap3d1, itsn1, arhgap21*, and *atp6v1b1)* disrupts Vangl2 localization in the TE septum. Scale bars are 50 µm (20µm in insets).

Mutation of EA/TEF patient-like genes in *Xenopus* disrupts Rab11-Vangl2 localization

We next assessed whether a similar mechanism was involved in the TEF observed when we mutated the *Xenopus* orthologs of endosome pathway risk genes from patients. We tested

400 *AP3D1*, *ARHGAP21*, and *ITSN1* which encode adaptors and CDC42-GEFs respectively during
401 endocytic vesicle formation, as well as *ATP6V1B1*, which encodes a vacuolar ATPase subunit
402 required for acidification of endosomal vesicles[34-38]. As predicted, F0 CRISPR mutants of *ap3d1*,
403 *arhgap21*, *atp6v1b1* and *itsn1* all exhibited a loss of apical Vangl2 localization and a
404 disorganized persistent septum (Figure 6O-R), consistent with these proteins functioning in the
405 recycling endosome pathway.
406
407 Together these results indicate that during tracheoesophageal morphogenesis, dynamic
408 recycling endosome activity is required to localize Vangl2 at the cell surface where the opposing
409 midline epithelia adhere to one another. Vangl2 appears to define an "apical memory" in the
410 epithelial bilayer cells which have lost aPKC and upregulate Cadherin, a membrane
411 configuration more typical of adherent basal-lateral cell-cell contacts. This unexpected behavior
412 is distinct from the typical roles for Vangl2 in apical-basal and planar cell polarity.
413
414 **Loss of Vangl or Celsr disrupts tracheoesophageal morphogenesis resulting in TEF**
415 The results above imply that Vangl-Celsr is required for tracheoesophageal morphogenesis.
416 Interestingly, one patient from our EA/TEF cohort had a heterozygous *de novo* damaging
417 missense variant in *CELSR2* predicted to alter an amino acid (N953S) in an N-terminal cadherin
418 domain[23,39]. Moreover, a rare *de novo* variant in *CELSR1* (V1452I) was previously reported in
419 another EA/TEF patient[40]. Together with our observations that cell polarity is disrupted in
420 endosome mutants, this led us to test whether Vangl-Celsr were required for trachea-
421 esophageal morphogenesis in *Xenopus*.
422
423 Loss of function CRISPR-Cas9 F0 *Xenopus* mutants for *celsr2*, *celsr1,* or *vangl2* all resulted in
424 variably penetrant TEF in 25-30% of the embryos at NF44 (Table 1). Examination of the mutant
425 foreguts at NF40 revealed a disorganized, thicker septum with round cells in the middle and
426 frequent blisters, phenocopying the endosome mutants (Figure 7A-D). Moreover, the *celsr1 and*
427 *celsr2* mutants exhibited reduced Vangl2 immunostaining, consistent with previous reports that
428 Celsr1 forms a heterotypic cell-cell complex with Vangl2[28]. Interestingly, in *vangl2* and *celsr1/2*
429 mutants Rab11a was still localized to the middle of the bilayer (Figure 7E-H), indicating that
430 Vangl-Celsr complexes are required for tracheoesophageal morphogenesis downstream of
431 recycling endosomes. Together, these results suggest that an unexpected but evolutionarily
432 conserved endosome-cell polarity pathway controls tracheoesophageal morphogenesis and that
433 disruptions to this process might contribute to EA/TEF in many patients (Figure 7I).
434
435

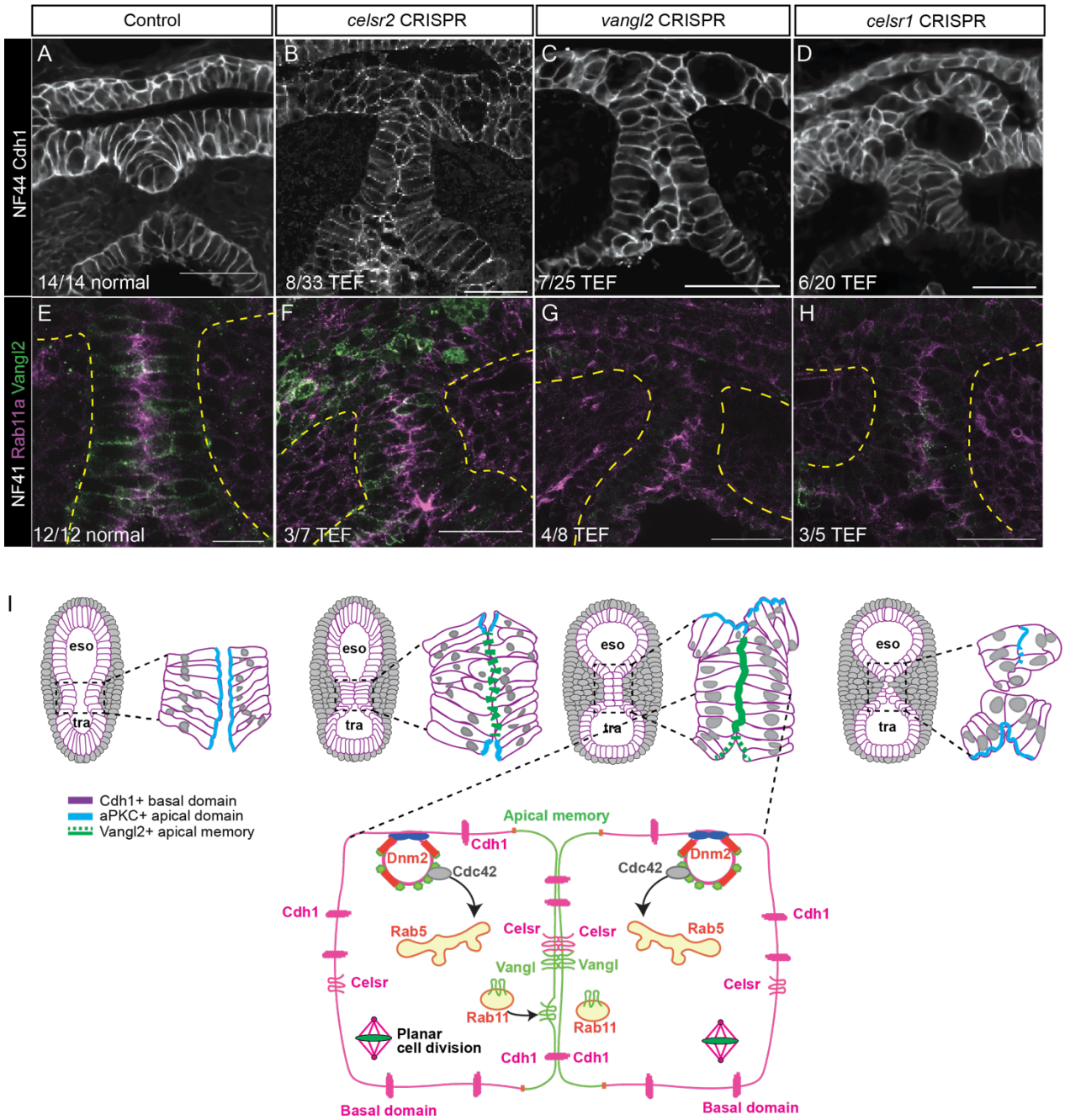

Fig. 7. Loss of Vangl or Celsr disrupts tracheoesophageal morphogenesis, resulting in TEF. (A-D) Cdh1 immunostaining in *celsr2*, *vangl2*, and *celsr1* mutants with TEF (E-H) disorganized epithelial septa that fail to co-localize Vangl2-Rab11a. Scale bars are 50 µm. I) Model of how endosome trafficking of Vangl2 maintains apical-basal polarity information and the proper tissue organization required for tracheoesophageal morphogenesis.

Discussion

In this study, we demonstrate that an endosome-cell polarity pathway is required for the epithelial remodeling that drives *Xenopus* tracheoesophageal morphogenesis. We discovered that Rab11+ recycling endosomes localize the transmembrane polarity protein Vangl2 to the

contact surface where foregut epithelia fuse. This appears to confer an “apical memory” which is essential to maintain an organized transient epithelial bilayer and its subsequent fission into distinct trachea and esophagus (Figure 7I). This unexpected Rab11-Vangl2 activity is distinct from its typical roles in planar cell polarity and apical basal polarity, and may represent a general paradigm for epithelial fusion and fission during morphogenesis.

Our study provides new insight into how cell and tissue polarity is regulated during tissue fusion and fission through endosome-mediated dynamic relocation of polarity and cell adhesion proteins. Previous work suggests that the hierarchy of endosome trafficking and cell polarity in development is context dependent. In the fetal mouse epidermis, endosomes internalize Vangl, Celsr, and Fzd proteins organized along the proximal-distal axis in typical PCP fashion, which are later relocated back to the appropriate cell surface after cell division to maintain epithelial organization[31]. In contrast, Vangl2 functions upstream of Rab11 in classical Wnt/PCP and apical-basal polarity roles to regulate convergent extension, planar cell polarization and apical constriction during Xenopus gastrulation and neural tube morphogenesis[41-43]. We show in the foregut that Rab11a is upstream of Vangl2, as Rab11a is still localized properly in vangl/celsr F0 CRISPR mutants. We propose that Vangl2 confers “apical memory” to cells that have otherwise lost apical character. The Vangl-Vangl interface is unexpected since in most other reports, Vangl-Celsr interactions are heterotypic, with Vangl+ cells binding to Celsr+ / Vangl- cells. In addition, we find no evidence of Vangl-mediated PCP activity during tracheoesophageal morphogenesis. Another distinction between what we have described in the foregut and these other examples of Vangl-regulated epithelial morphogenesis is that in the foregut the epithelia first fuses (like the neural tube and palate) but then undergo fission. Other tissues that experience this type of dynamic fusion-fission morphogenesis include separation of anorectal tubes in the hindgut and semicircular canals in the ear[44-46]. We predict that similar Rab11a-Vangl2 mechanisms may act in those tissues.

We also show a role for Vangl2 that is distinct from its typical functions in apical-basal polarity. Our observation that Vangl2 and Rab11a colocalize coincident with a loss of Par3 and aPKC in the foregut bilayer epithelium was unexpected since Vangl2 is typically thought to help recruit these proteins to the apical surface in a polarized epithelium. There is precedence for Vangl2 activity independent of its classical polarity roles. In the developing mouse pancreas, apical restriction of Vangl2 maintains epithelial integrity independent of apical-basal cell polarity[47]. Vangl2 also has cell shape and polarity functions in the developing mouse lung mesenchyme during branching morphogenesis independent of its PCP or apical-basal polarity roles[48,49]. Neither the *looptail* mutation (dominant-negative) nor conditional knockout of Vangl2 using

484 ShhCre impairs trachea-esophageal separation. We postulate that a different Cre driver with
485 earlier recombination in the foregut might lead to separation anomalies. The observation that
486 endosomal mutants have a TEF penetrance of ~60% while Vangl-Celsr F0 mutants only have a
487 30% penetrance suggests there may be genetic redundancy (Rab11a vs Rab11b) and Vangl
488 family members (Vangl1 vs Vangl2). Redundancy between Rab11a/b was shown in the
489 developing mouse pancreas, as knockout of both Rab11a and Rab11b was required to see
490 epithelial defects[50]. Another possibility is that in addition to Vangl2, other endosome cargo
491 proteins participate in foregut morphogenesis.
492
493 Cadherin is a candidate cargo of recycling endosomes in the foregut. Unlike Vangl2, Cdh1 can
494 still localize to the midline of the fused epithelial bilayer in endosome mutants. However, we
495 show that Cdh1 needs to be internalized by endocytosis at the separating epithelial cell surface
496 for fission of the bilayer into the trachea and esophagus. We postulate that other endosomal
497 cargo may include Integrins that facilitate tissue adhesion and Laminins that mediate interaction
498 with the adjacent mesoderm at the basal surface. Consistent with this possibility, we note that
499 EA/TEF patients were identified with potentially damaging variants in *ITGB4* and *LAMB4*[23].
500 Another candidate pathway that might regulate endosome-mediated loss of adhesion is the
501 Eph/Ephrin pathway. Eph/Ephrin are known to regulate tissue separation and cell sorting in
502 many contexts[51] and *Efnb2* was recently shown to be required for trachea-esophageal
503 separation downstream of Nkx2-1[52,53]. In the future we will test the intriguing possibility that
504 Ephrin-Cadherin-endosome-Vangl interactions mediate tissue adhesion and separation in the
505 developing foregut.
506
507 Endosome trafficking is a ubiquitous cell pathway required for homeostasis and many basic
508 cellular functions. Several pleiotropic diseases are associated with variants in endosome
509 trafficking genes[22], but interestingly many of these are rather specific to certain tissues. Not
510 surprisingly, total loss of endosome activity leads to early embryonic lethality in germline mutant
511 mice[54,55] and in *Xenopus* embryos results in gastrulation and neurulation defects[41]. Our F0
512 CRISPR mutagenesis on the other hand results in 58-90% indel mutations, more damaged than
513 a heterozygote but not complete nulls. Indeed, in our experiments, endosome mutant embryos
514 have a significantly higher frequency of gastrulation and neurulation defects compared to
515 controls where the pigmentation gene *tyr* was mutated. In our experiments we selected those
516 embryos that survived to later stages. The fact that later embryos with partial loss of endosome
517 activity show specific defects suggests that developing organs and tissue undergoing dynamic
518 epithelial remodeling, like tracheoesophageal separation, represent developmental bottlenecks
519 that are particularly sensitive to disruptions in endosomal trafficking. This may partially explain

520 why EA/TEF patients frequently present with variants predicted to have partial loss of function or
521 hypomorphic variants in endosome and polarity pathway genes.
522
523 Our results are consistent with the “saddle rising” model of trachea-esophageal separation
524 proposed by Que and colleagues[4] and provide a cellular basis for the saddle as the point of
525 epithelial fusion-fission and mesenchymal invasion. We note differences between *Xenopus* and
526 mouse TE morphology and anatomy – in mice, the epithelial fusion event is more transient and
527 only 3-4 cells in length, while in *Xenopus*, the epithelial fusion event is more prolonged, forming
528 a bilayer septum tissue over 10 cells in length[14]. In mammals the foregut tissue significantly
529 grows in the longitudinal plane as the trachea and esophagus separate resulting in an apparent
530 “rising” of the saddle compared to *Xenopus*. Our study uses *Xenopus* as a model to perform
531 rapid disease causality screening and cellular analysis to minimize the confounding issue of
532 tissue growth.
533
534 The EA/TEF risk genes validated in this study are involved in various stages of endosome
535 trafficking, including vesicle formation (ITSN1, AP1G2), cytoskeletal transport (ARHGAP21,
536 ABRA, RASAL2, RAPGEF3), vesicle acidification (ATP6V1B1) [23,40]. Interestingly the patients
537 enriched in endosome variants frequently had co-morbidities similar to those observed in
538 patients with VANGL1/2 mutations [28] such as neural tube anomalies[56,57], renal anomalies[58,59],
539 congenital heart anomalies[60,61], and lung diseases[62]. While further studies are required to test a
540 causal link between endosome and polarity proteins in patients, it is tempting to speculate that
541 complex EA/TEF patients tend to have comorbidities in organs that experience tissue fusion-
542 fission during fetal development[23]. This suggests the provocative possibility of an
543 "endosomeopathy" syndrome, similar to ciliopathies. Further comparative analysis of patient
544 genetics and animal models will deepen our understanding of tissue fusion and fission events
545 during development, aiding the care and treatment of patients.
546
547 Limitations of the study
548 The F0 CRISPR-Cas9 gene editing strategy used in our study is inherently variable compared to
549 analyzing germline mutants. We took advantage of rapid *Xenopus* embryonic development to
550 efficiently screen patient risk genes generating simple indels that produced loss of function
551 mutations. However, it is possible that variants in EA/TEF patients result in missense gain of
552 function or hypomorphic proteins. Moreover, the available evidence suggests that EA/TEF risk is
553 polygenic and our approach does not account for this. Indeed, we found that some of the gene
554 mutations resulted in a low penetrance TEF, which was not significant over controls, but might

555 indicate a contribute to the phenotyope in a polygenic state. Future studies should model the
556 patient's variants and consider multiple genes acting together.
557
558 We also do not rule out the possibility that endosome trafficking is required in the surrounding
559 mesenchyme. This might include polarized secretion of matrix metalloproteases for basement
560 membrane degradation or PCP-mediated directional mesenchyme migration across the midline
561 during trachea-esophageal separation. Follow up studies using tissue-specific manipulations will
562 be necessary to address this possibility.
563

564 **Acknowledgements**
565 We thank the Bio-Imaging and Analysis Facility for imaging and analysis advice
566 (RRID:SCR_022628), the Division of Veterinary Services, and the DNA Sequencing Core at
567 CCHMC (RRID:SCR_022630) for their services used in this study. We thank S. Sokol for kindly
568 providing the anti-Vangl2 antibody. We thank the resources provided by the National Xenopus
569 Resource (RRID:NXR_0012) and Xenbase (RRID:SCR_003280)[63]. We thank the members of
570 the CLEARconsortium.org for access to EA/TEF patient data and for helpful discussions. This
571 work is supported by NICHD P01HD093393 to YS, WKC, and AMZ, and a Canadian Institutes
572 of Health Research postdoctoral fellowship to NAE. This project was supported in part by NIH
573 P30 DK078392 of the Digestive Diseases Research Core Center in Cincinnati for the Bio-
574 Imaging and Analysis Facility and the DNA Sequencing Core at CCHMC.
575

576 **Author contributions**
577 Conceptualization: NAE, AMZ. Formal analysis: NAE, AK, AMZ. Funding acquisition: YS, WKC,
578 AMZ. Investigation: NAE, SAR, AK, AW, ZA, APK. Methodology: NAE, SAR, MJK. Project
579 administration: NAE, AMZ. Supervision: NAE, AMZ. Validation: NAE. Visualization: NAE, AMZ.
580 Writing – original draft: NAE, AMZ. Writing – review & editing: all authors.
581

582 **Declaration of interests**
583 The authors declare no competing interests.
584

585 **Methods**
586 **Experimental models**
587 *Xenopus* experiments were performed using Cincinnati Children's Hospital Medical Center
588 (CCHMC) Institutional Animal Care and Use Committee (IACUC 2022-0026) approved
589 guidelines. Wild type adult *Xenopus tropicalis* and *Xenopus laevis* frogs were purchased from

590 NASCO and Xenopus1 (USA) and housed in the CCHMC vivarium under standard housing
591 conditions. *Xenopus* embryos were obtained by *in vitro* fertilization according to standard
592 procedures[64]. Transgenic membrane GFP *Xenopus laevis*
593 (*Xla.Tg(CMV:memGFP;cryga:mCherry)*^{NXR}) were purchased from the National Xenopus
594 Resource (RRID:NXR_0012). *Sox2* germline mutant embryos were generated at the National
595 *Xenopus* Resource according to standard procedures (RRID:SCR_013731).
596
597 **CRISPR-Cas9 gene editing and Xenopus embryo culture**
598 Guide RNAs and genotyping primers were designed using CRISPRScan, InDelphi, and
599 CRISPOR predictive algorithms[65] and synthesized as altR-cRNA by IDT (sequences in
600 Resources Table and Table S3). Guide RNA sequences that maximized predictive efficiency
601 (CRISPRScan) and high percentage of predicted out of frame indel mutations (InDelphi) were
602 selected. After annealing with tracrRNA to create a single gRNA, gRNAs were combined with
603 recombinant Cas9 protein (PNA Biosciences) and injected into 1-2 cell stage *Xenopus* embryos
604 at a final concentration of 500-700pg gRNA and 1-1.5ng Cas9p. *Xenopus tropicalis* embryos
605 were raised at 25°C in 0.1X Modified Barth's solution (MBS) for three days post fertilization
606 before being anesthetized and fixed at NF44 in MEMFA (3.7% formaldehyde, 0.1M MOPS, 2mM
607 EGTA, 1mM $MgSO_4$) for 1hr at room temperature, then in Dent's solution (80% methanol, 20%
608 DMSO) for long term storage at -20°C. *Xenopus laevis* embryos were raised between 15-21°C
609 in 0.1X MBS for 3-5 days post fertilization (to stages NF37-44), then anesthetized and fixed in
610 MEMFA or 2% trichloroacetic acid (for endosome proteins and Vangl2 immunostaining) for 30-
611 40 mins at room temperature. Embryos were immunostained and imaged by confocal
612 microscopy as outlined below prior to genotyping.
613
614 **Genotype-phenotype scoring**
615 Genotyping for CRISPR-Cas9 editing efficiency in individual CRISPR-edited embryos was
616 performed as described in Zhong et al., 2022[23] using the primer sequences in Resources Table
617 and Table S3. PCR amplified products from individual embryos were sent for Sanger
618 sequencing at the DNA Sequencing Facility at CCHMC. Sanger sequences were deconvoluted
619 using Inference of CRISPR Edits (Synthego, USA) or Tracking of Indels by Decomposition,
620 TIDE, Brinkman et al., 2014[66]) to determine percent indel efficiency (percent of mutations in
621 each embryo) and mosaicism (different types of indel mutations in a given embryo) (Figure S1).
622 Only embryos with >40% indel efficiency were considered in genotype-phenotype analysis, as if
623 the mutation burden was less than this, we concluded that the gene was not sufficiently mutated
624 to test its function. A minimum of 20 individual mutant embryos from 3 independent editing
625 experiments were analyzed to identify a statistically significant frequency of trachea-esophageal

626 anomalies by Student's t-test from the 2% baseline detected in controls. Individual genotype-
627 phenotype scoring and mutation efficiency are provided in Table S2.
628
629 **E-Cadherin site-directed mutagenesis and *Xenopus* transgenesis**
630 pCS2+ *Xenopus* E-cadherin-3xGFP was a gift from Ann Miller (University of Michigan) and
631 described in Higashi et al 2016[67]. A dileucine motif (LL) in the evolutionarily conserved juxta-
632 membrane cytoplasmic domain of E-cadherin is required for E-cadherin endocytosis[27]. Site-
633 directed mutagenesis was performed with the GeneArt Mutagenesis kit (ThermoFisher A13282
634 with Accuprime Taq Polymerase, ThermoFisher12339016) using the following primers (mutant
635 sequence bold, underlined; wt sequence TTA CTA encodes LL, mutation GCA GCG encodes AA
636 to mutate these two leucines (LL) at positions 732, 733 into alanines (AA) of Xenopus E-
637 cadherin.

638 Forward mutagenic primer:
639 5'- GTG GTA AAA GAG CCT **GCA GCG** CCT CCA GAA GGC GAC -3'
640 Reverse Mutagenic primer:
641 3'- CAC CAT TTT CTC GGA **CGT CGC** GGA GGT CTT CCG CTG -5'
642
643 Mutagenesis was confirmed with the following sequencing primers:
644 Forward sequencing primer: 5' GAG CTG GAG ATT GGT CAA TAC G 3' ;
645 Reverse sequencing primer: 5' GAG CCA CTG CCT TCA TAA TCG 3'.
646
647 Following confirmation of mutagenesis, both the Cdh1-GFP wild type and mutant (LL>AA) were
648 cloned into the pCR8-Gateway TOPO vector (ThermoFisher K250020) according to
649 manufacturer's instructions. Gateway LR Clonase II Plus (Thermo Scientific #12538120) was
650 then used in standard recombination reactions according to manufacturer's instructions to
651 transfer the *EcadGFP wild type and mutant (LL>AA)* into the pDXTRE transgenesis
652 responder plasmid[68], which enables Dox-dependent expression.
653
654 Transgenic embryos were generated as follows: 250pg of pDXTP-*hhex* promoter:rtTA (Nasr et
655 al., 2019[14]) and 500pg of pDXTR-EcadGFP (wt or LL>AA mutant) were incubated in a 25uL
656 reaction containing 2.5µL of I-SceI meganuclease enzyme (New England Biolabs #R0694S) in
657 0.5X I-SceI buffer. The reaction was incubated at 37°C for 40 minutes and then 5nL of this
658 reaction mix was immediately injected into 1-cell embryos on either side of the sperm entry point
659 within the first 60-75 minutes after fertilization. Embryos were cultured at 13-15°C for the first two
660 to three hours after injection and subsequently at 18°C to 23°C degrees thereafter. Transgenic

661 embryos were selected based on GFP fluorescence in the eye, which becomes visible during
662 early tailbud stages[68]. Transgenes were activated by the addition of doxycycline (Sigma #D9891)
663 at a final concentration of 50µg/mL to the embryo culture buffer (0.1X MBS). Culturing of un-
664 injected embryos in this dose of Dox has no noticeable effect on embryonic development nor
665 tracheal-esophageal separation. Transgenic efficiency (embryos with GFP+ eyes at tailbud
666 stages NF33-35) ranged from approximately 8% to 16%, consistent with previous transgenic
667 studies[14,68].
668
669 **Whole mount immunostaining and confocal microscopy**
670 Whole mount immunostaining on *Xenopus* tissue was performed as described in Nasr et al.,
671 2019[14] and Zhong et al., 2022[23] with the following modifications for imaging endosome and
672 polarity proteins: fixed embryos were rehydrated in PBS, embedded in 2% low melt agarose in
673 PBS, and sectioned with a Vibratome VT1000S (Leica) to obtain 200 µm tissue slices containing
674 the trachea and esophagus. Slices were permeabilized with 0.1% Triton X-100 in PBS (0.3%
675 Triton X-100 for anti-Vangl2), blocked in 5% normal donkey serum in PBS, then incubated in
676 primary antibody (1:100) in blocking solution overnight at 4°C. Slices were incubated in Alexa
677 fluor-conjugated secondary antibody (1:500) in blocking solution for 2 hours at room
678 temperature, then dehydrated in 100% methanol. For confocal microscopy, slices were cleared
679 in BABB and imaged on a Nikon A1 inverted laser scanning confocal microscope with a 10X,
680 20X water immersion, or 40X oil immersion objective (Nikon USA). For super resolution
681 microscopy, slices were cleared in BABB and imaged on a Nikon AXR confocal microscope with
682 spatial array detector (NSPARC, Nikon, USA) in super resolution mode with a 40X and 100X oil
683 immersion objective.
684
685 **Image analyses**
686 *Signal intensity quantification*: Signal intensity quantification was performed in ImageJ (NIH).
687 Regions of interest (ROI) were drawn around the apical and basal membranes, then mean gray
688 value was measured and plotted as mean intensity ± max/min normalized to the fluorescence
689 intensity of memGFP signal. At least five cells were measured per embryo in a minimum of five
690 embryos per condition for quantification and statistical analysis by 2W-ANOVA.
691
692 *Prolate ellipticity, surface contact area, and 3D quantification of Cdh1*: Prolate ellipticity and
693 surface contact area measurements were performed in Imaris (Bitplane). 3D cell volumes were
694 rendered based on E-Cadherin staining and surface models were generated. Prolate ellipticity
695 was measured from rendered surfaces of epithelial cells and plotted as mean ± max/min. Values
696 approaching 1 have elongated shapes while values approaching 0 have spherical shapes.

697 Surface-surface contact area between the esophagus and trachea-esophageal septum, within
698 the trachea-esophageal septum, and between the trachea and trachea-esophageal septum was
699 measured from rendered surfaces of epithelial cells using the Surface-Surface Contact Area
700 XTension and plotted as the mean ± max/min. Mean Cdh1 intensity was measured on the
701 rendered surface. At least five cells were measured per embryo in a minimum of five embryos
702 per condition for quantification and statistical analysis by unpaired Student's t-test (prolate
703 ellipticity) and 1W-ANOVA (surface contact area).
704
705 *Three-dimensional measurements of axes in the foregut*: Three dimensional lengths of x
706 (medial), y (dorsal-ventral), and z (rostral-caudal) axes were performed in Imaris (Bitplane). 3D
707 cell volumes were rendered based on E-Cadherin staining and surface models were generated.
708 Lengths were measured from rendered surfaces of epithelial cells and plotted as the mean
709 length of each axis ± standard error of the mean. At least five embryos were measured for
710 quantification and statistical analysis by unpaired Student's t-test.
711
712 *Mitotic spindle orientation*: Mitotic spindle orientation angles were obtained in ImageJ (NIH) as
713 described in Franco and Carmena, 2019[69]. Only images with z-sections through the axial axis of
714 *Xenopus* embryos containing clearly identifiable mitotic spindles stained with anti-α-tubulin were
715 analyzed for spindle angles. One line of the angle was drawn through linking both centrosomes,
716 and the second line of the angle was drawn parallel to the basement membrane of the epithelial
717 cell. Measurements were collected and wind rose plots were generated in Excel. At least three
718 mitotic spindles were measured in a minimum of 5 embryos for quantification and statistical
719 analysis was performed by Kolmogorov-Smirnov tests.
720
721 *Colocalization and nearest neighbor analysis (super resolution)*: Pearson colocalization
722 coefficients between Vangl2/Rab11a, Cdh1/Rab11a, and Celsr1/Rab11a immunostaining signals
723 were calculated in Nikon Elements (Nikon USA). ROIs were drawn around an entire cell, and
724 the Pearson colocalization coefficient was determined. A coefficient of 1 indicates two channels
725 whose fluorescence intensities are perfectly linearly related. For super resolution imaging
726 quantification, Rab11a and Vangl2 spots were detected and rendered in Imaris (Bitplane USA).
727 Distances between Rab11a-Vangl2 spots were measured and graphed as a histogram. Vangl2
728 spots within 500nm of Rab11a spots were considered to be within the Rab11a+ recycling
729 endosome compartment[32,33]. At least six cells were measured in a minimum of 5 embryos for
730 quantification and statistical analyses by 1W-ANOVA.
731

732 **Immunoblotting**

733 Whole Xenopus embryos or microdissected anterior foregut tissue (from pharynx to stomach)
734 were pooled and lysed in Triton X-100 lysis buffer (0.5% Triton X-100, 0.1M HEPES, 150 mM
735 NaCl, 2mM EDTA pH 8.0, 2mM EGTA) containing protease inhibitors (ThermoFisher). Protein
736 lysates were combined with 2X Laemmli buffer and 0.1M DTT, boiled, and separated by 4-12%
737 Bis-Tris gel electrophoresis (ThermoFisher). For HRP detection, membranes were blocked in
738 5% BSA, then incubated in primary antibody (1:1000) overnight in blocking solution at 4°C.
739 Membranes were incubated in HRP-conjugated secondary antibody (1:5000) in blocking
740 solution for 1 hour at room temperature, then visualized by addition of ECL substrate
741 (Amersham, GE) and imaged using a ChemiDoc (BioRad). Western blot quantification was
742 performed in ImageLab (BioRad).

743

744 **Resources**

745

Antibodies		
Rabbit anti-PKC zeta	Abcam	ab59364; RRID:AB_944858
Mouse anti-Cdh1	Developmental Studies Hybridoma Bank	5D3 (deposited to the DSHB by Gumbiner, B.M.); RRID:AB_528116
Rabbit anti-Dnm2	Abcam	Ab65556; RRID:AB_1603781
Rabbit anti-Rab5a	Cell Signaling Technology	3547; RRID:AB_2300649
Rabbit anti-Rab11a	Thermo Fisher Scientific	700184; RRID:AB_2532295
Mouse anti-Rab11a	BD Biosciences	610657; RRID:AB_397984
Rabbit anti-Tjp1 (ZO-1)	Thermo Fisher Scientific	61-7300; RRID:AB_138452
Rabbit anti-Par3	Millipore	07-330; RRID:AB_2101325
Mouse anti-Tuba4b	Sigma	T9026; RRID:AB_477593
Rabbit anti-Lama1	Sigma	L9393; RRID:AB_477163
Rabbit anti-pHH3 (Ser10)	Cell Signaling Technology	9701; RRID:AB_331535
Rabbit anti-Vangl2	S. Sokol lab	RRID:AB_2744499
Rabbit anti-Celsr1	BiCell Scientific	50801
Mouse anti-Sox2	Abcam	ab79351; RRID:AB_10710406
Rabbit anti-Nkx2-1	Santa Cruz	sc-13040; RRID:AB_793532
Goat anti-Foxf1	R&D Systems	AF4798; RRID:AB_2105588
Rabbit anti-Itsn1	Millipore	ABS984
Donkey anti-mouse AF488	ThermoFisher Scientific	A-21202
Donkey anti-goat AF568	ThermoFisher Scientific	A-11057

Donkey anti-rabbit AF647	ThermoFisher Scientific	A-31573
Donkey anti-rabbit AF568	ThermoFisher Scientific	A10042
Donkey anti-mouse AF647	ThermoFisher Scientific	A-31571
Chemicals		
Cas9 protein	PNA Biosciences	CP01-50
Doxycycline hyclate	Sigma	D9891
GeneArt Mutagenesis Kit	ThermoFisher Scientific	A13282
Accuprime Taq	ThermoFisher Scientific	12339016
pCR8-Gateway TOPO vector	ThermoFisher Scientific	K250020
Gateway LR Clonase II Plus	ThermoFisher Scientific	12538120
I-SceI	New England Biolabs	R0694S
Normal donkey serum	Jackson Immuno Research Laboratories	017-000-121
Experimental models: organisms/strains		
Xenopus laevis females	NASCO	LM00531
Xenopus laevis males	NASCO	LM00715
Xenopus tropicalis females	Xenopus1	
Xenopus tropicalis males	Xenopus1	
Xenopus laevis: Xla.Tg(CMV:memGFP;cryga:mCherry)^{NXR}	National Xenopus Resource	NXR_0012
Xenopus tropicalis sox2 mutant embryos	National Xenopus Resource	NXR_3051; Xtr.sox2^{tmHorb}
Oligonucleotides *(See Table S3 for all sequences)*		
Rab11a.S gRNA GAGATTACTCTTCCCCACAC	IDT	Nasr et al., 2019[14]
Rab5a gRNA CGACTGCAGATTCTCCTAAA	IDT	This study
Dnm2 gRNA CGGAGACCGAGTGCAGCCAT	IDT	This study
Slc45a2 gRNA GGTTACATAGGCTGCCTCCA	IDT	Delay et al., 2018[70]
Genotyping, Rab11a.S forward primer	IDT	This study

ACAGTGTGCATAGAATTTGGCG		
Genotyping, Rab11a.S reverse primer CGTGTGTTGCCTAGAGGGAC	IDT	This study
Genotyping, Dnm2.S forward primer GGAGCCAGCGAGAAACACTTA	IDT	This study
Genotyping, Dnm2.S reverse primer GCGACAATATCAACCCACCAA	IDT	This study
Genotyping, Dnm2.L forward primer AGGGAAACACTTACCGGCCTA	IDT	This study
Genotyping, Dnm2.L reverse primer GAAACACAACCAATCACAATCCCT	IDT	This study
Genotyping, Rab5a.S forward primer ACCCTGGCAAACTTTGTGGT	IDT	This study
Genotyping, Rab5a.L forward primer GAGCATCCAACCCACCCTTT		This study
Genotyping, Rab5a reverse primer ACTGTCCCTTTACGAAGCGA	IDT	This study
Software and online tools		
NIS Elements	Nikon	RRID:SCR_014329
ImageJ	NIH	RRID:SCR_003070
IMARIS	Oxford Instruments	RRID:SCR_007370
Surface-Surface Contact Area XTension	Oxford Instruments	https://imaris.oxinst.com/open/view/surface-surface-contact-area
Prism 9	GraphPad	RRID:SCR_002798
Inference of CRISPR edits (ICE)	Synthego	http://www.ice.synthego.com
Tracking of Indels by Decomposition (TIDE)	Van Steensel Lab (Netherlands Cancer Institute)	https://tide.nki.nl
InDelphi	Gifford Lab (MIT)	https://indelphi.giffordlab.mit.edu
CRISPRScan	Giraldez Lab (Yale)	https://www.crisprscan.org
CRISPOR		https://crispor.gi.ucsc.edu
ImageLab	BioRad	RRID:SCR_014210

747 **References**

748 1. Edwards, N.A., Shacham-Silverberg, V., Weitz, L., Kingma, P.S., Shen, Y., Wells, J.M.,
749 Chung, W.K., and Zorn, A.M. (2021). Developmental basis of trachea-esophageal birth
750 defects. Dev Biol *477*, 85-97. 10.1016/j.ydbio.2021.05.015.
751 2. Raad, S., David, A., Que, J., and Faure, C. (2020). Genetic Mouse Models and Induced
752 Pluripotent Stem Cells for Studying Tracheal-Esophageal Separation and Esophageal
753 Development. Stem Cells Dev *29*, 953-966. 10.1089/scd.2020.0075.
754 3. van Lennep, M., Singendonk, M.M.J., Dall'Oglio, L., Gottrand, F., Krishnan, U.,
755 Terheggen-Lagro, S.W.J., Omari, T.I., Benninga, M.A., and van Wijk, M.P. (2019).
756 Oesophageal atresia. Nat Rev Dis Primers *5*, 26. 10.1038/s41572-019-0077-0.
757 4. Zhang, Y., Jiang, M., Kim, E., Lin, S., Liu, K., Lan, X., and Que, J. (2017). Development
758 and stem cells of the esophagus. Semin Cell Dev Biol *66*, 25-35.
759 10.1016/j.semcdb.2016.12.008.
760 5. Chitkara, A.E., Tadros, M., Kim, H.J., and Harley, E.H. (2003). Complete
761 laryngotracheoesophageal cleft: complicated management issues. Laryngoscope *113*,
762 1314-1320. 10.1097/00005537-200308000-00010.
763 6. Bednarczyk, D., Sasiadek, M.M., and Smigiel, R. (2013). Chromosome aberrations and
764 gene mutations in patients with esophageal atresia. J Pediatr Gastroenterol Nutr *57*,
765 688-693. 10.1097/MPG.0b013e3182a373dc.
766 7. Stoll, C., Alembik, Y., Dott, B., and Roth, M.P. (2017). Associated anomalies in cases
767 with esophageal atresia. Am J Med Genet A *173*, 2139-2157. 10.1002/ajmg.a.38303.
768 8. Brosens, E., Ploeg, M., van Bever, Y., Koopmans, A.E., H, I.J., Rottier, R.J., Wijnen, R.,
769 Tibboel, D., and de Klein, A. (2014). Clinical and etiological heterogeneity in patients with
770 tracheo-esophageal malformations and associated anomalies. Eur J Med Genet *57*,
771 440-452. 10.1016/j.ejmg.2014.05.009.
772 9. Li, Y., Litingtung, Y., Ten Dijke, P., and Chiang, C. (2007). Aberrant Bmp signaling and
773 notochord delamination in the pathogenesis of esophageal atresia. Dev Dyn *236*, 746-
774 754. 10.1002/dvdy.21075.
775 10. Goss, A.M., Tian, Y., Tsukiyama, T., Cohen, E.D., Zhou, D., Lu, M.M., Yamaguchi, T.P.,
776 and Morrisey, E.E. (2009). Wnt2/2b and beta-catenin signaling are necessary and
777 sufficient to specify lung progenitors in the foregut. Dev Cell *17*, 290-298.
778 10.1016/j.devcel.2009.06.005.

11. Harris-Johnson, K.S., Domyan, E.T., Vezina, C.M., and Sun, X. (2009). beta-Catenin promotes respiratory progenitor identity in mouse foregut. Proc Natl Acad Sci U S A *106*, 16287-16292. 10.1073/pnas.0902274106.
12. Rankin, S.A., Han, L., McCracken, K.W., Kenny, A.P., Anglin, C.T., Grigg, E.A., Crawford, C.M., Wells, J.M., Shannon, J.M., and Zorn, A.M. (2016). A Retinoic Acid-Hedgehog Cascade Coordinates Mesoderm-Inducing Signals and Endoderm Competence during Lung Specification. Cell Rep *16*, 66-78. 10.1016/j.celrep.2016.05.060.
13. Kim, E., Jiang, M., Huang, H., Zhang, Y., Tjota, N., Gao, X., Robert, J., Gilmore, N., Gan, L., and Que, J. (2019). Isl1 Regulation of Nkx2.1 in the Early Foregut Epithelium Is Required for Trachea-Esophageal Separation and Lung Lobation. Dev Cell *51*, 675-683 e674. 10.1016/j.devcel.2019.11.002.
14. Nasr, T., Mancini, P., Rankin, S.A., Edwards, N.A., Agricola, Z.N., Kenny, A.P., Kinney, J.L., Daniels, K., Vardanyan, J., Han, L., et al. (2019). Endosome-Mediated Epithelial Remodeling Downstream of Hedgehog-Gli Is Required for Tracheoesophageal Separation. Dev Cell *51*, 665-674 e666. 10.1016/j.devcel.2019.11.003.
15. Cote, L.E., and Feldman, J.L. (2022). Won't You be My Neighbor: How Epithelial Cells Connect Together to Build Global Tissue Polarity. Front Cell Dev Biol *10*, 887107. 10.3389/fcell.2022.887107.
16. Pickett, M.A., Naturale, V.F., and Feldman, J.L. (2019). A Polarizing Issue: Diversity in the Mechanisms Underlying Apico-Basolateral Polarization In Vivo. Annu Rev Cell Dev Biol *35*, 285-308. 10.1146/annurev-cellbio-100818-125134.
17. Runck, L.A., Method, A., Bischoff, A., Levitt, M., Pena, A., Collins, M.H., Gupta, A., Shanmukhappa, S., Wells, J.M., and Guasch, G. (2014). Defining the molecular pathologies in cloaca malformation: similarities between mouse and human. Dis Model Mech *7*, 483-493. 10.1242/dmm.014530.
18. Aigouy, B., and Le Bivic, A. (2016). The PCP pathway regulates Baz planar distribution in epithelial cells. Sci Rep *6*, 33420. 10.1038/srep33420.
19. Murdoch, J.N., Doudney, K., Paternotte, C., Copp, A.J., and Stanier, P. (2001). Severe neural tube defects in the loop-tail mouse result from mutation of Lpp1, a novel gene involved in floor plate specification. Hum Mol Genet *10*, 2593-2601. 10.1093/hmg/10.22.2593.
20. Butler, M.T., and Wallingford, J.B. (2018). Spatial and temporal analysis of PCP protein dynamics during neural tube closure. Elife *7*. 10.7554/eLife.36456.

812 21. Torban, E., Wang, H.J., Patenaude, A.M., Riccomagno, M., Daniels, E., Epstein, D., and
813 Gros, P. (2007). Tissue, cellular and sub-cellular localization of the Vangl2 protein during
814 embryonic development: effect of the Lp mutation. Gene Expr Patterns *7*, 346-354.
815 10.1016/j.modgep.2006.07.007.
816 22. Yarwood, R., Hellicar, J., Woodman, P.G., and Lowe, M. (2020). Membrane trafficking in
817 health and disease. Dis Model Mech *13*. 10.1242/dmm.043448.
818 23. Zhong, G., Ahimaz, P., Edwards, N.A., Hagen, J.J., Faure, C., Lu, Q., Kingma, P.,
819 Middlesworth, W., Khlevner, J., El Fiky, M., et al. (2022). Identification and validation of
820 candidate risk genes in endocytic vesicular trafficking associated with esophageal
821 atresia and tracheoesophageal fistulas. HGG Adv *3*, 100107.
822 10.1016/j.xhgg.2022.100107.
823 24. Szklarczyk, D., Kirsch, R., Koutrouli, M., Nastou, K., Mehryary, F., Hachilif, R., Gable,
824 A.L., Fang, T., Doncheva, N.T., Pyysalo, S., et al. (2023). The STRING database in
825 2023: protein-protein association networks and functional enrichment analyses for any
826 sequenced genome of interest. Nucleic Acids Res *51*, D638-D646.
827 10.1093/nar/gkac1000.
828 25. Nakayama, T., Fish, M.B., Fisher, M., Oomen-Hajagos, J., Thomsen, G.H., and Grainger,
829 R.M. (2013). Simple and efficient CRISPR/Cas9-mediated targeted mutagenesis in
830 Xenopus tropicalis. Genesis *51*, 835-843. 10.1002/dvg.22720.
831 26. Guo, X., Zhang, T., Hu, Z., Zhang, Y., Shi, Z., Wang, Q., Cui, Y., Wang, F., Zhao, H., and
832 Chen, Y. (2014). Efficient RNA/Cas9-mediated genome editing in Xenopus tropicalis.
833 Development *141*, 707-714. 10.1242/dev.099853.
834 27. Miyashita, Y., and Ozawa, M. (2007). Increased Internalization of p120-uncoupled E-
835 cadherin and a Requirement for a Dileucine Motif in the Cytoplasmic Domain for
836 Endocytosis of the Protein. Journal of Biological Chemistry *282*, 11540-11548.
837 10.1074/jbc.M608351200.
838 28. Butler, M.T., and Wallingford, J.B. (2017). Planar cell polarity in development and
839 disease. Nat Rev Mol Cell Biol *18*, 375-388. 10.1038/nrm.2017.11.
840 29. Panzica, D.A., Findlay, A.S., van Ladesteijn, R., and Collinson, J.M. (2019). The core
841 planar cell polarity gene, Vangl2, maintains apical-basal organisation of the corneal
842 epithelium. J Anat *234*, 106-119. 10.1111/joa.12676.

843 30. vandenBerg, A.L., and Sassoon, D.A. (2009). Non-canonical Wnt signaling regulates cell
844 polarity in female reproductive tract development via van gogh-like 2. Development *136*,
845 1559-1570. 10.1242/dev.034066.
846 31. Devenport, D., Oristian, D., Heller, E., and Fuchs, E. (2011). Mitotic internalization of
847 planar cell polarity proteins preserves tissue polarity. Nat Cell Biol *13*, 893-902.
848 10.1038/ncb2284.
849 32. Ecker, M., Redpath, G.M.I., Nicovich, P.R., Rossy, J., and Lippincott-Schwartz, J. (2021).
850 Quantitative visualization of endocytic trafficking through photoactivation of fluorescent
851 proteins. Molecular Biology of the Cell *32*, 892-902. 10.1091/mbc.E20-10-0669.
852 33. Puri, C., Vicinanza, M., Ashkenazi, A., Gratian, M.J., Zhang, Q., Bento, C.F., Renna, M.,
853 Menzies, F.M., and Rubinsztein, D.C. (2018). The RAB11A-Positive Compartment Is a
854 Primary Platform for Autophagosome Assembly Mediated by WIPI2 Recognition of PI3P-
855 RAB11A. Developmental Cell *45*, 114-131.e118. 10.1016/j.devcel.2018.03.008.
856 34. Yang, Q., Li, G., Singh, S.K., Alexander, E.A., and Schwartz, J.H. (2006). Vacuolar H+ -
857 ATPase B1 subunit mutations that cause inherited distal renal tubular acidosis affect
858 proton pump assembly and trafficking in inner medullary collecting duct cells. J Am Soc
859 Nephrol *17*, 1858-1866. 10.1681/ASN.2005121277.
860 35. Dong, X., Li, H., Derdowski, A., Ding, L., Burnett, A., Chen, X., Peters, T.R., Dermody,
861 T.S., Woodruff, E., Wang, J.J., and Spearman, P. (2005). AP-3 directs the intracellular
862 trafficking of HIV-1 Gag and plays a key role in particle assembly. Cell *120*, 663-674.
863 10.1016/j.cell.2004.12.023.
864 36. Kantheti, P., Qiao, X., Diaz, M.E., Peden, A.A., Meyer, G.E., Carskadon, S.L.,
865 Kapfhamer, D., Sufalko, D., Robinson, M.S., Noebels, J.L., and Burmeister, M. (1998).
866 Mutation in AP-3 delta in the mocha mouse links endosomal transport to storage
867 deficiency in platelets, melanosomes, and synaptic vesicles. Neuron *21*, 111-122.
868 10.1016/s0896-6273(00)80519-x.
869 37. Dubois, T., Paléotti, O., Mironov, A.A., Fraisier, V., Stradal, T.E., De Matteis, M.A.,
870 Franco, M., and Chavrier, P. (2005). Golgi-localized GAP for Cdc42 functions
871 downstream of ARF1 to control Arp2/3 complex and F-actin dynamics. Nat Cell Biol *7*,
872 353-364. 10.1038/ncb1244.
873 38. Gryaznova, T., Gubar, O., Burdyniuk, M., Kropyvko, S., and Rynditch, A. (2018).
874 WIP/ITSN1 complex is involved in cellular vesicle trafficking and formation of filopodia-
875 like protrusions. Gene *674*, 49-56. 10.1016/j.gene.2018.06.078.

876 39. Wang, J., Ahimaz, P.R., Hashemifar, S., Khlevner, J., Picoraro, J.A., Middlesworth, W.,
877 Elfiky, M.M., Que, J., Shen, Y., and Chung, W.K. (2021). Novel candidate genes in
878 esophageal atresia/tracheoesophageal fistula identified by exome sequencing. Eur J
879 Hum Genet *29*, 122-130. 10.1038/s41431-020-0680-2.
880 40. Zhang, R., Gehlen, J., Kawalia, A., Melissari, M.T., Dakal, T.C., Menon, A.M., Hofele, J.,
881 Riedhammer, K., Waffenschmidt, L., Fabian, J., et al. (2020). Human exome and mouse
882 embryonic expression data implicate ZFHX3, TRPS1, and CHD7 in human esophageal
883 atresia. PLoS One *15*, e0234246. 10.1371/journal.pone.0234246.
884 41. Lee, J.Y., and Harland, R.M. (2010). Endocytosis is required for efficient apical
885 constriction during Xenopus gastrulation. Curr Biol *20*, 253-258.
886 10.1016/j.cub.2009.12.021.
887 42. Ossipova, O., Kim, K., Lake, B.B., Itoh, K., Ioannou, A., and Sokol, S.Y. (2014). Role of
888 Rab11 in planar cell polarity and apical constriction during vertebrate neural tube
889 closure. Nat Commun *5*, 3734. 10.1038/ncomms4734.
890 43. Ossipova, O., Chuykin, I., Chu, C.W., and Sokol, S.Y. (2015). Vangl2 cooperates with
891 Rab11 and Myosin V to regulate apical constriction during vertebrate gastrulation.
892 Development *142*, 99-107. 10.1242/dev.111161.
893 44. Seifert, A.W., Harfe, B.D., and Cohn, M.J. (2008). Cell lineage analysis demonstrates an
894 endodermal origin of the distal urethra and perineum. Developmental Biology *318*, 143-
895 152. 10.1016/j.ydbio.2008.03.017.
896 45. Martin, P., and Swanson, G.J. (1993). Descriptive and Experimental Analysis of the
897 Epithelial Remodellings That Control Semicircular Canal Formation in the Developing
898 Mouse Inner Ear. Developmental Biology *159*, 549-558. 10.1006/dbio.1993.1263.
899 46. Alsina, B., and Whitfield, T.T. (2017). Sculpting the labyrinth: Morphogenesis of the
900 developing inner ear. Seminars in Cell & Developmental Biology *65*, 47-59.
901 10.1016/j.semcdb.2016.09.015.
902 47. Flasse, L., Yennek, S., Cortijo, C., Barandiaran, I.S., Kraus, M.R., and Grapin-Botton, A.
903 (2020). Apical Restriction of the Planar Cell Polarity Component VANGL in Pancreatic
904 Ducts Is Required to Maintain Epithelial Integrity. Cell Rep *31*, 107677.
905 10.1016/j.celrep.2020.107677.
906 48. Paramore, S.V., Trenado-Yuste, C., Sharan, R., Nelson, C.M., and Devenport, D. (2024).
907 Vangl-dependent mesenchymal thinning shapes the distal lung during murine
908 sacculation. Developmental Cell *59*, 1302-1316.e1305. 10.1016/j.devcel.2024.03.010.

909 49. Paramore, S.V., Goodwin, K., Fowler, E.W., Devenport, D., and Nelson, C.M. (2024).
910 Mesenchymal Vangl1 and Vangl2 facilitate airway elongation and widening
911 independently of the planar cell polarity complex. Development *151*.
912 10.1242/dev.202692.
913 50. Barlow, H.R., Ahuja, N., Bierschenk, T., Htike, Y., Fassetta, L., Azizoglu, D.B., Flores, J.,
914 Gao, N., De la, O.S., Sneddon, J.B., et al. (2023). Rab11 is essential to pancreas
915 morphogenesis, lumen formation and endocrine mass. Dev Biol *499*, 59-74.
916 10.1016/j.ydbio.2023.05.002.
917 51. Niethamer, T.K., and Bush, J.O. (2019). Getting direction(s): The Eph/ephrin signaling
918 system in cell positioning. Developmental Biology *447*, 42-57.
919 10.1016/j.ydbio.2018.01.012.
920 52. Lewis, A.E., Kuwahara, A., Franzosi, J., and Bush, J.O. (2022). Tracheal separation is
921 driven by NKX2-1-mediated repression of Efnb2 and regulation of endodermal cell
922 sorting. Cell Rep *38*, 110510. 10.1016/j.celrep.2022.110510.
923 53. Lewis, A.E., Hwa, J., Wang, R., Soriano, P., and Bush, J.O. (2015). Neural crest defects
924 in ephrin-B2 mutant mice are non-autonomous and originate from defects in the
925 vasculature. Developmental Biology *406*, 186-195. 10.1016/j.ydbio.2015.08.021.
926 54. Yu, S., Yehia, G., Wang, J., Stypulkowski, E., Sakamori, R., Jiang, P., Hernandez-
927 Enriquez, B., Tran, T.S., Bonder, E.M., Guo, W., and Gao, N. (2014). Global ablation of
928 the mouse Rab11a gene impairs early embryogenesis and matrix metalloproteinase
929 secretion. J Biol Chem *289*, 32030-32043. 10.1074/jbc.M113.538223.
930 55. Ferguson, S.M., Raimondi, A., Paradise, S., Shen, H., Mesaki, K., Ferguson, A.,
931 Destaing, O., Ko, G., Takasaki, J., Cremona, O., et al. (2009). Coordinated actions of
932 actin and BAR proteins upstream of dynamin at endocytic clathrin-coated pits. Dev Cell
933 *17*, 811-822. 10.1016/j.devcel.2009.11.005.
934 56. Iliescu, A., Gravel, M., Horth, C., and Gros, P. (2014). Independent mutations at Arg181
935 and Arg274 of Vangl proteins that are associated with neural tube defects in humans
936 decrease protein stability and impair membrane targeting. Biochemistry *53*, 5356-5364.
937 10.1021/bi500400g.
938 57. Merello, E., Mascelli, S., Raso, A., Piatelli, G., Consales, A., Cama, A., Kibar, Z., Capra,
939 V., and Marco, P.D. (2015). Expanding the mutational spectrum associated to neural
940 tube defects: literature revision and description of novel VANGL1 mutations. Birth
941 Defects Res A Clin Mol Teratol *103*, 51-61. 10.1002/bdra.23305.

942 58. Papakrivopoulou, E., Vasilopoulou, E., Lindenmeyer, M.T., Pacheco, S., Brzóska, H.,
943 Price, K.L., Kolatsi-Joannou, M., White, K.E., Henderson, D.J., Dean, C.H., et al. (2018).
944 Vangl2, a planar cell polarity molecule, is implicated in irreversible and reversible kidney
945 glomerular injury. J Pathol *246*, 485-496. 10.1002/path.5158.
946 59. Schnell, U., and Carroll, T.J. (2016). Planar cell polarity of the kidney. Exp Cell Res *343*,
947 258-266. 10.1016/j.yexcr.2014.11.003.
948 60. Yuan, Y., Gao, Y., Wang, H., Ma, X., Ma, D., and Huang, G. (2014). Promoter
949 methylation and expression of the VANGL2 gene in the myocardium of pediatric patients
950 with tetralogy of fallot. Birth Defects Res A Clin Mol Teratol *100*, 973-984.
951 10.1002/bdra.23291.
952 61. Li, D., and Wang, J. (2018). Planar Cell Polarity Signaling in Mammalian Cardiac
953 Morphogenesis. Pediatr Cardiol *39*, 1052-1062. 10.1007/s00246-018-1860-5.
954 62. Yates, L.L., and Dean, C.H. (2011). Planar polarity: A new player in both lung
955 development and disease. Organogenesis *7*, 209-216. 10.4161/org.7.3.18462.
956 63. Fisher, M., James-Zorn, C., Ponferrada, V., Bell, A.J., Sundararaj, N., Segerdell, E.,
957 Chaturvedi, P., Bayyari, N., Chu, S., Pells, T., et al. (2023). Xenbase: key features and
958 resources of the Xenopus model organism knowledgebase. Genetics *224*.
959 10.1093/genetics/iyad018.
960 64. Wlizla, M., McNamara, S., and Horb, M.E. (2018). Generation and Care of Xenopus
961 laevis and Xenopus tropicalis Embryos. Methods Mol Biol *1865*, 19-32. 10.1007/978-1-
962 4939-8784-9_2.
963 65. Naert, T., Tulkens, D., Edwards, N.A., Carron, M., Shaidani, N.I., Wlizla, M., Boel, A.,
964 Demuynck, S., Horb, M.E., Coucke, P., et al. (2020). Maximizing CRISPR/Cas9
965 phenotype penetrance applying predictive modeling of editing outcomes in Xenopus and
966 zebrafish embryos. Sci Rep *10*, 14662. 10.1038/s41598-020-71412-0.
967 66. Brinkman, E.K., Chen, T., Amendola, M., and van Steensel, B. (2014). Easy quantitative
968 assessment of genome editing by sequence trace decomposition. Nucleic Acids
969 Research *42*, e168-e168. 10.1093/nar/gku936.
970 67. Higashi, T., Arnold, Torey R., Stephenson, Rachel E., Dinshaw, Kayla M., and Miller,
971 Ann L. (2016). Maintenance of the Epithelial Barrier and Remodeling of Cell-Cell
972 Junctions during Cytokinesis. Current Biology *26*, 1829-1842.
973 10.1016/j.cub.2016.05.036.

974 68. Sterner, Z.R., Rankin, S.A., Wlizla, M., Choi, J.A., Luedeke, D.M., Zorn, A.M., and
975 Buchholz, D.R. (2019). Novel vectors for functional interrogation of Xenopus ORFeome
976 coding sequences. genesis *57*. 10.1002/dvg.23329.
977 69. Franco, M., and Carmena, A. (2019). Measurement of Mitotic Spindle Angle and Mitotic
978 Cell Distance in Fixed Tissue of Drosophila Larval Brains. Bio Protoc *9*, e3432.
979 10.21769/BioProtoc.3432.
980 70. DeLay, B.D., Corkins, M.E., Hanania, H.L., Salanga, M., Deng, J.M., Sudou, N., Taira,
981 M., Horb, M.E., and Miller, R.K. (2018). Tissue-Specific Gene Inactivation in Xenopus
982 laevis: Knockout of lhx1 in the Kidney with CRISPR/Cas9. Genetics *208*, 673-686.
983 10.1534/genetics.117.300468.
984

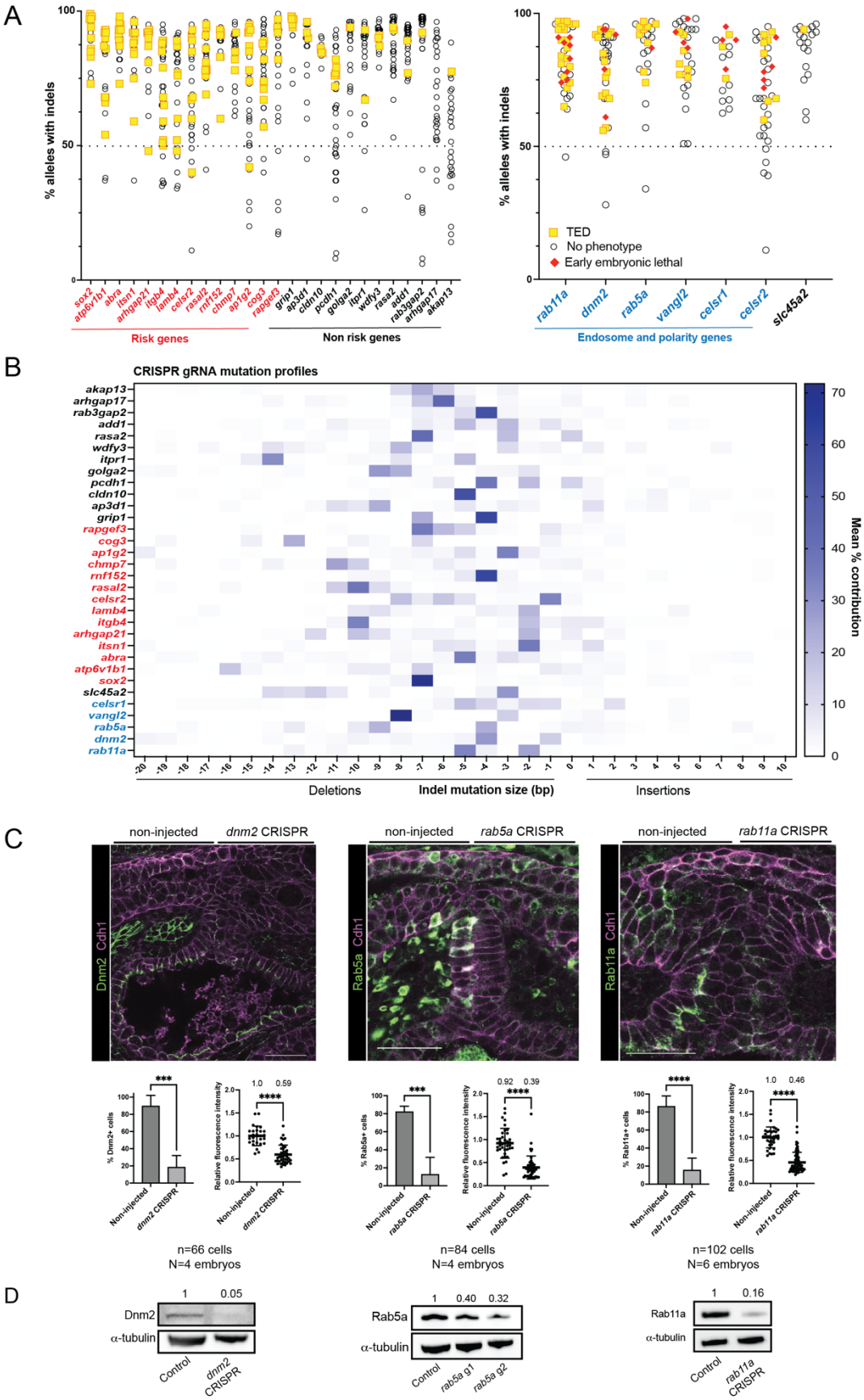
A
% alleles with indels
Risk genes
Non risk genes
TED
No phenotype
Early embryonic lethal
Endosome and polarity genes
B
CRISPR gRNA mutation profiles
Mean % contribution
Deletions
Indel mutation size (bp)
Insertions
C
non-injected
dnm2 CRISPR
rab5a CRISPR
rab11a CRISPR
Dnm2 Cdh1
Rab5a Cdh1
Rab11a Cdh1
n=66 cells
N=4 embryos
n=84 cells
N=4 embryos
n=102 cells
N=6 embryos
D
Dnm2
α-tubulin
Control
dnm2 CRISPR
Rab5a
rab5a g1
rab5a g2
Rab11a
rab11a CRISPR

985

986
987 **Supplemental Figure 1 (Related to Figure 1) F0 CRISPR-Cas9 editing strategy generates**
988 **highly edited embryos.** A) Left: Graph demonstrating correlation between editing efficiency (%
989 alleles with indels) and phenotype penetrance in embryos with mutations in patient risk genes.
990 Right: Graph shows the correlation between editing efficiency, embryonic lethality, and phenotype
991 penetrance in embryos with mutations in endosome and polarity genes. B) Heat map displaying
992 the frequency and types of indel mutations generated by the indicated gRNA in F0 embryo, mean
993 of n=5-15 individual embryo Sanger sequencing analysis per gRNA. C) Immunostaining and
994 confocal microscopy of unilaterally-injected tadpoles at the 2-cell stage with dnm2, rab5a, or
995 rab11a CRISPR reagents and quantification of reduced number of protein-expressing cells and
996 protein abundance on the injected side of the tadpole compared to the control, non-injected side.
997 Graphs are mean ± SEM, ***$p<0.001$, ****$p<0.0001$ Students' t-test, numbers above dot plots are
998 the mean. D) Immunoblotting of foreguts dissected from Xenopus CRISPR mutants compared to
999 controls. Relative protein abundance indicated by numbers above immunoblots, with control
1000 protein abundance normalized to 1.
1001

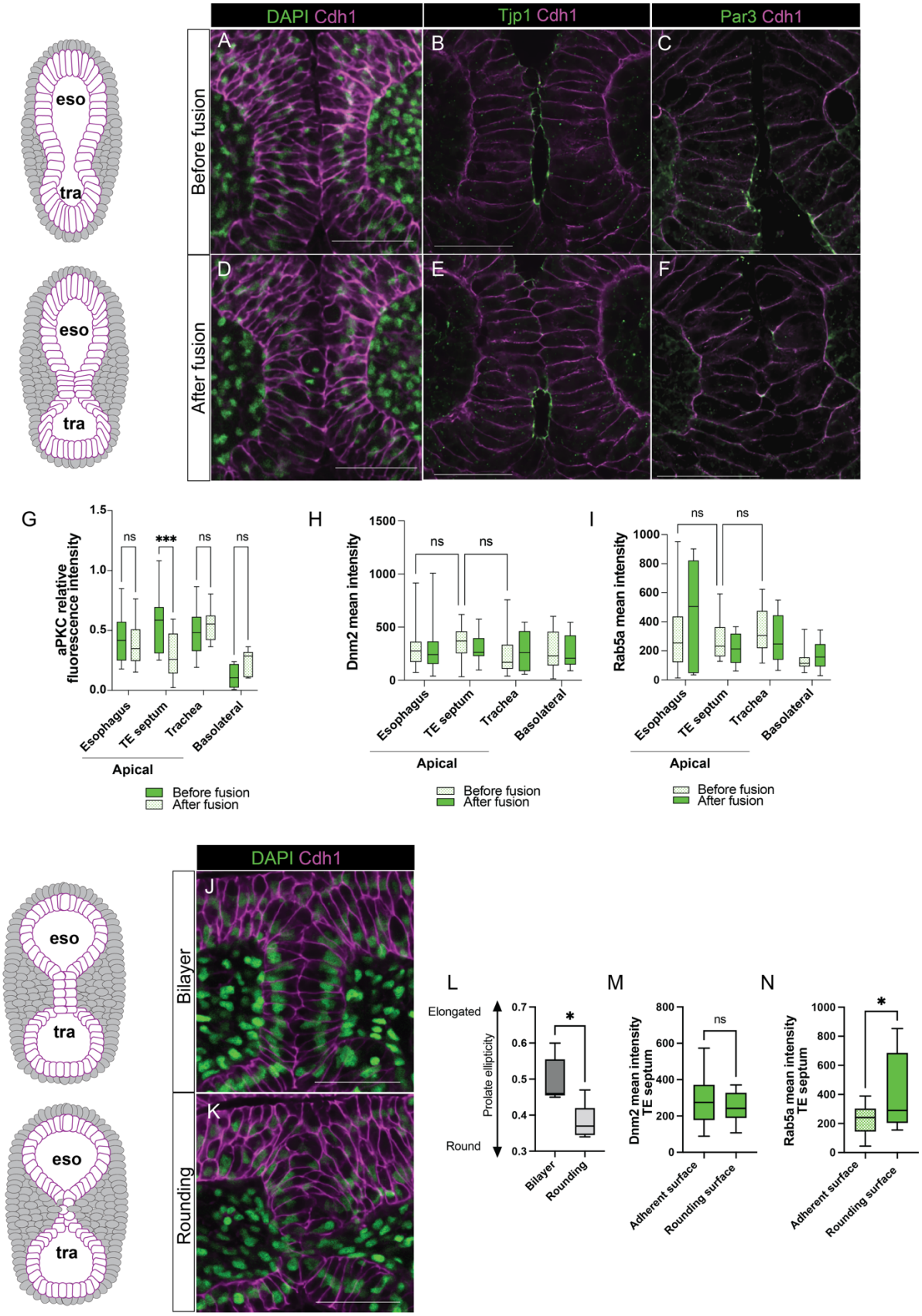
DAPI Cdh1
Tjp1 Cdh1
Par3 Cdh1
Before fusion
After fusion
eso
tra
A
B
C
D
E
F
G
aPKC relative fluorescence intensity
ns
***
Esophagus
TE septum
Trachea
Basolateral
Apical
Before fusion
After fusion
H
Dnm2 mean intensity
I
Rab5a mean intensity
DAPI Cdh1
Bilayer
Rounding
J
K
L
Elongated
Round
Prolate ellipticity
Bilayer
Rounding
M
Dnm2 mean intensity TE septum
Adherent surface
Rounding surface
N
Rab5a mean intensity TE septum

1002

1003 **Supplemental Figure 2 (Related to Figure 2) Dynamic cell shape and polarity changes**
1004 **during trachea-esophageal separation**. A-C) Before fusion the foregut is a pseudostratified
1005 epithelium with apical tight junctions (Tjp1) and Par3. D-F) After apical fusion, epithelial cells
1006 remodel to localize E-Cadherin (Cdh1) apically and downregulate Tjp1 and Par3. G)
1007 Quantification of aPKC downregulation after epithelial fusion (mean ± min/max, ****$p<0.00001$,
1008 2W-ANOVA, n=6 cells per embryo, N=5 embryos). H) Quantification of Dnm2 intensity after
1009 epithelial fusion (mean ± min/max, 2W-ANOVA, n=6 cells per embryo, N=5 embryos). I)
1010 Quantification of Rab5a intensity after epithelial fusion (mean ± min/max, 2W-ANOVA, n=6 cells
1011 per embryo, N=5 embryos). J) Before resolution of the septum, the foregut epithelium remodels
1012 to a bilayered columnar epithelium with basally positioned nuclei. K) The septum resolves after
1013 downregulation of E-Cadherin and integration of septum cells into either the trachea or
1014 esophagus. L) Prolate ellipticity is significantly decreased in cells actively resolving in the
1015 septum (mean ± min/max, *$p<0.05$, Student's t-test, n=6 cells per embryo, N=5 embryos). M)
1016 Quantification of Dnm2 intensity before and after resolution (mean ± min/max, Student's t-test,
1017 n=6 cells per embryo, N=5 embryos) N) Quantification of Rab5a intensity before and after
1018 resolution (mean ± min/max, *$p<0.05$, Student's t-test, n=6 cells per embryo, N=5 embryos).

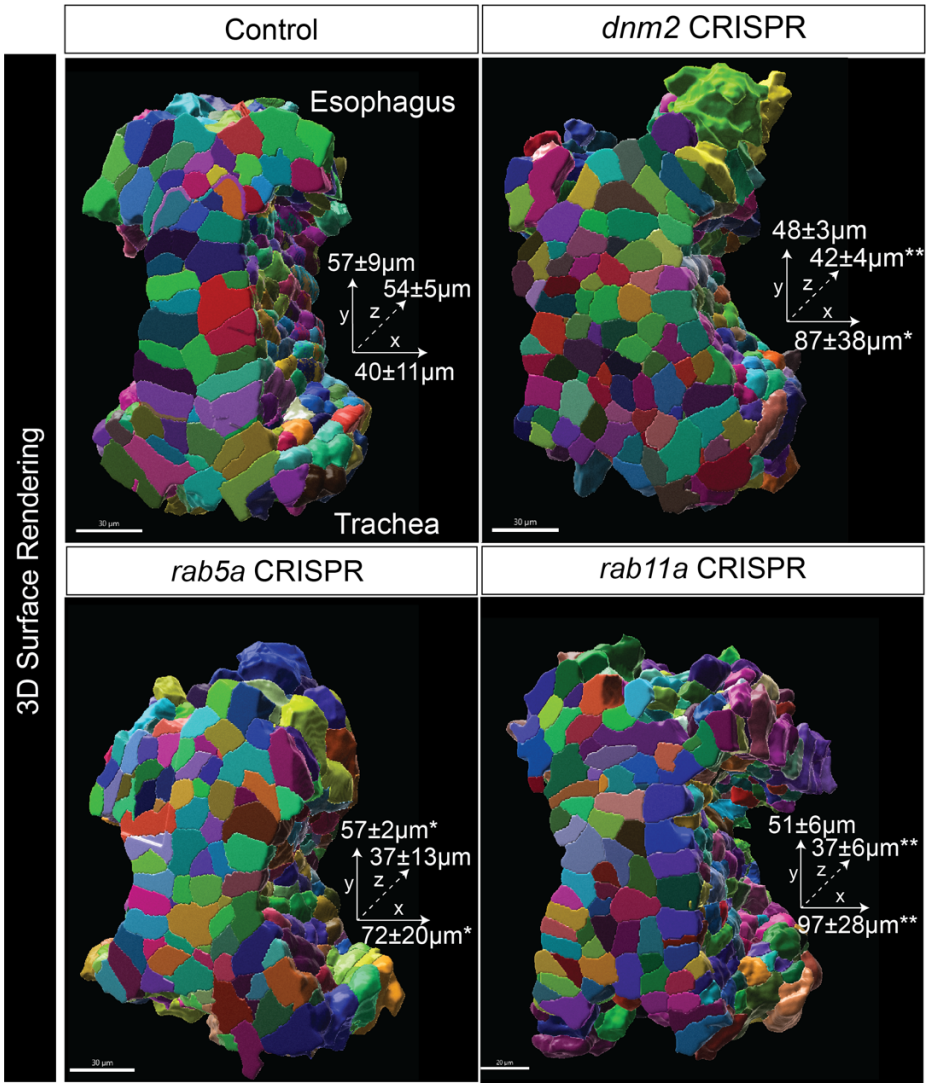

Supplemental Figure 4 (Related to Figure 4) 3D surface renderings and measurements of the epithelial septum showing that mutants are significantly wider (x axis) and shorter in the rostral-caudal (z axis) axis compared to controls (mean length ± SEM, Student's t-test compared to control lengths, *p<0.05, **p<0.01, n=4-6 embryos per condition). Scale bars are 30 µm.

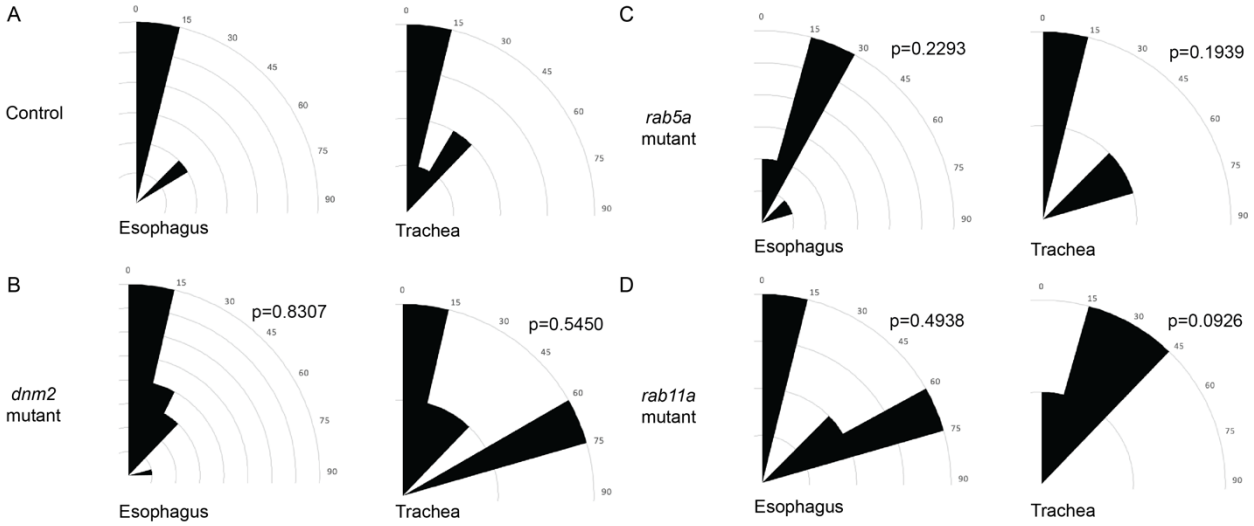

Supplemental Figure 5 (Related to Figure 5). Mitotic spindle angles are not significantly changed compared to controls in the trachea and esophageal epithelia of endosome mutants. A) Control embryo trachea and esophagus epithelia most frequently divide between 0-15°C relative to the plane of the tissue. B-D) Endosome mutant trachea and esophagus epithelia division angles are not significantly altered, but trend to be more variable than control trachea and esophageal epithelia (Kolmogorov-Smirnov test, n.s. $p>0.05$, 3-5 cells measured per embryo, 5 embryos measured per condition).

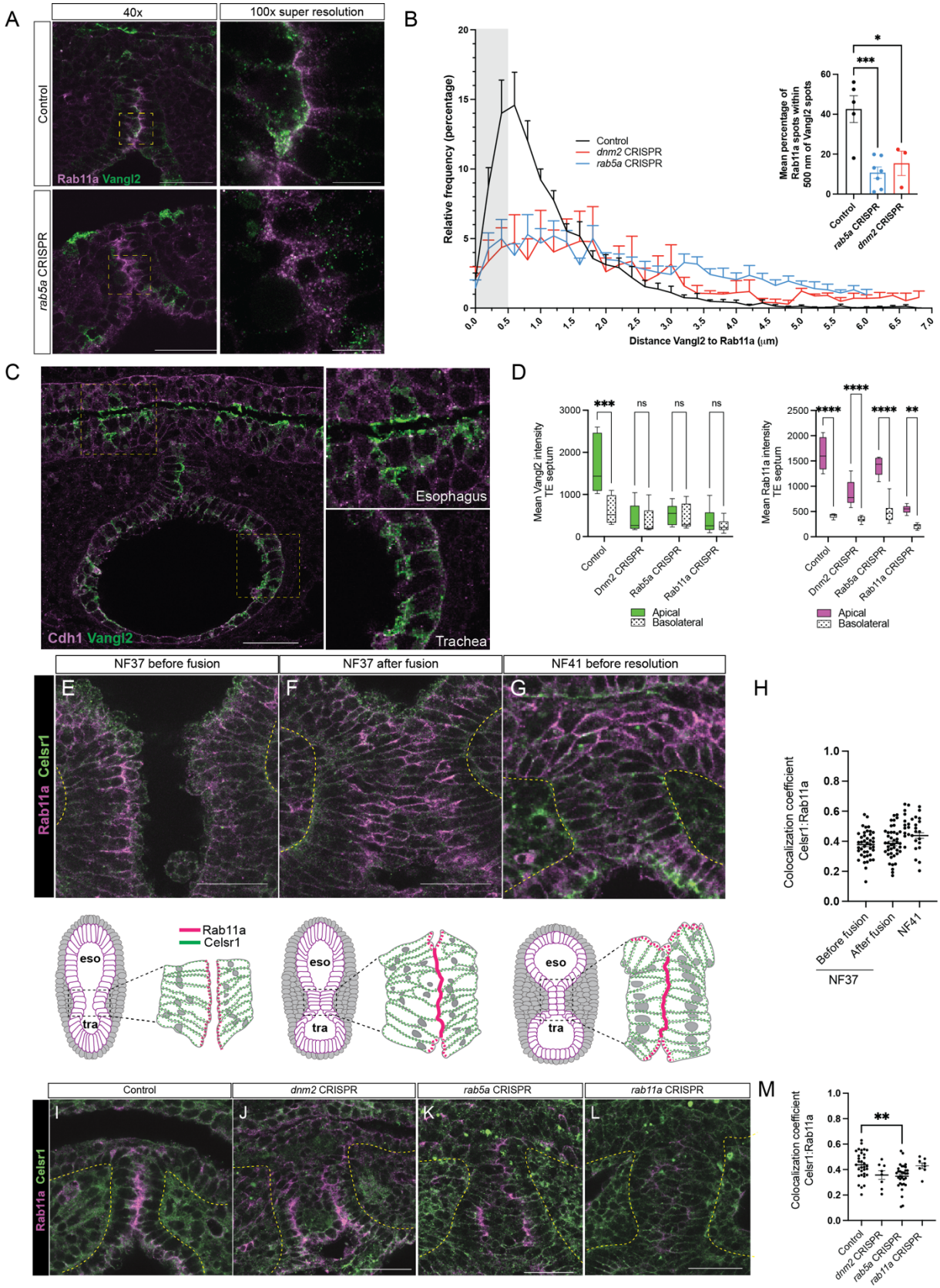
A
40x
100x super resolution
Control
rab5a CRISPR
Rab11a Vangl2
B
Relative frequency (percentage)
Control
dnm2 CRISPR
rab5a CRISPR
Distance Vangl2 to Rab11a (µm)
Mean percentage of Rab11a spots within 500 nm of Vangl2 spots
Control
rab5a CRISPR
dnm2 CRISPR
C
Cdh1 Vangl2
Esophagus
Trachea
D
Mean Vangl2 intensity TE septum
Mean Rab11a intensity TE septum
Control
Dnm2 CRISPR
Rab5a CRISPR
Rab11a CRISPR
Apical
Basolateral
NF37 before fusion
NF37 after fusion
NF41 before resolution
E
F
G
H
Rab11a Celsr1
Rab11a
Celsr1
eso
tra
Colocalization coefficient Celsr1:Rab11a
Before fusion
After fusion
NF41
NF37
Control
dnm2 CRISPR
rab5a CRISPR
rab11a CRISPR
I
J
K
L
M

878

879 **Supplemental Figure 6 (Related to Figure 6) Celsr1 is localized to the periphery of cells**
880 **during tracheoesophageal separation.** A) Super-resolution confocal of Rab11a-Vangl2
881 immunostaining in representative control and Rab5a CRISPR mutant embryos. B) Quantification
882 of distance between Vangl2-Rab11a spots binned and plotted as relative frequency histograms.
883 Inset: mean percentage of Vangl2 spots within 500nm of Rab11a spots (area under curve in gray
884 box) mean ± SEM, N=3-7 embryos, *p<0.05. ***p<0.001 C) Immunostaining of Vangl2 in the
885 trachea and esophageal epithelium. Vangl2 is localized apically in the lumen-facing esophageal
886 epithelia but not in the more basal cell layers and is localized around the membrane periphery in
887 the single cell tracheal epithelium (insets). D) Vangl2 intensity at the apical membrane is
888 decreased in dnm2, rab5a, and rab11a CRISPR mutants, while Rab11a remains localized to the
889 apical membranes (mean ± min/max, 2W-ANOVA, ****p<0.0001, ***p<0.001, **p<0.01, n=3-5
890 cells per embryo, 5 embryos analyzed). E-H) Time course of Celsr1 immunostaining during
891 *Xenopus* trachea-esophageal morphogenesis. Diagrams depict Celsr1/Rab11a localization
892 during foregut separation. I-M) Celsr1:Rab11a colocalization is significantly decreased in *rab5a*
893 Xenopus mutants, but Celsr1 cellular localization is not significantly altered in *dnm2*, *rab5a*, *and*
894 *rab11a* Xenopus mutants (mean ± min/max, 1W-ANOVA, **p<0.01. n=3-5 cells, 5 embryos
895 analyzed).

***Xenopus* ortholog of patient gene**	**Protein Function**	**% Indel mutations** (mean ± SD)	**Mean frequency of trachea-esophageal defect** (±SEM, n, N, p value)	**Xenopus Phenotype**
sox2	Transcription factor	100% -germline null	100% (±0, 14, 2, p<0.0001)***	TEF – 14/14
sox2	Transcription factor	90%± 8.6	61% (±10, 18, 3, p<0.0001)***	TEF – 11/18
atp6v1b1	Intracellular transport	82%±11.5	40% (±19,30, 2, p=0.0024)**	TEF – 4/30 Occluded lumens – 9/30
abra^	Rho-actin regulation	90%±6.1	41% (±8, 29, 4, p=0.0009)**	TEF – 10/29 Occluded lumens – 4/29
itsn1^	Endocytosis, Cdc42 GEF	87%±8.2	42% (±13, 26, 3, p=0.0038)**	TEF – 6/26 Occluded lumens – 5/26
arhgap21^	Rho family GTPase	85%±12.0	39% (±7, 23, 4, p=0.0006)**	TEF – 5/23 Occluded lumens – 8/23
itgb4^	Integrin adhesion, putative cargo	72%±14.5	26% (±8, 43, 5, p=0.0063)**	TEF – 9/43 Occluded lumens – 4/43
lamb4	Laminin subunit	71%±17.5	28% (±19, 32, 3, p=0.0121)*	TEF - 9/32 Occluded lumens – 1/32
celsr2^	Cell polarity, putative cargo	72%±16	24% (±5, 33, 2, p=0.0041)**	TEF - 6/33 Occluded lumens – 2/33
rasal2	Ras GTPase-like	81%±11.9	34% (±2, 32, 3, p=0.0005)***	TEF - 5/32 Occluded lumens – 5/32
rnf152	E3 ubiquitin ligase	85% ±11.3	32% (±2, 25, 3, p=0.0002)***	TEF – 7/25 Occluded lumens – 2/25
chmp7	Late endosomes	84%±10	26% (±7, 25 ,3 p=0.0061)**	TEF - 6/25 Occluded lumens - 1/25
ap1g2^	Endocytosis	76%±22.1	23% (±3, 47, 5, p=0.0038)**	TEF – 7/47
cog3	ER-Golgi transport	79%±14.5	18% (±6, 47, 3 p=0.037)*	TEF - 9/47 Occluded lumens - 3/47
rapgef3^	Ras signaling	86%±13	15% (±3, 34, 3, p=0.0360)*	TEF – 4/34 Occluded lumens – 2/34
grip1	Scaffold protein	95%±4.5	17% (±8, 44, 3, p=0.0712)	
ap3d1	Intracellular transport	85%±13.8	15% (±7, 20, 2, p=0.0808)	-
cldn10	Tight junctions	78%±11.3	14% (±7, 34, 3, p=0.1106)	-
pcdh1^	Cell adhesion, putative cargo	72%±14	13% (±7,34, 3, p=0.1361)	-
golga2	Golgi transport	87%±10	12% (±3, 38, 3, p=0.0606)	
itpr1	Inositol triphosphate receptor	79%±17.5	8% (±14, 27, 3, p=0.4262)	-
wdfy3	Autophagy	90%±4	9% (±5, 31, 3, p=0.2680)	

rasa2	Ras GTPase	85%±11	9% (±8, 38, 4, p=0.1950)	-
add1	Cytoskeleton	87%±9.3	5% (±5, 39, 3, p=0.6608)	-
rab3gap2^	Endocytosis	88%±14.2	5% (±6, 34, 3, p=0.5948)	-
arhgap17^	Rho signaling	75%±16	4% (±4, 39, 5, p=0.7341)	-
akap13	Rho guanine exchange factor	58%±14.5	6% (±6, 29, 3 p=0.5165)	-
tyr (control)	Pigmentation	n/d	2% (±2, 36, 6)	-
Endosome/polarity genes	**Protein Function**	**% Indel mutations (mean ± SD)**	**Mean frequency of trachea-esophageal defect** (±SEM, n, N, p value)	**Xenopus Phenotype**
dnm2	Endocytosis	82%±17	70% (±6, 65, 16, p=0.0002)***	TEF – 45/65 Occluded lumens – 14/65
rab5a	Early endosome GTPase	79%±9	63% (±6, 78, 16, p=0.0004)***	TEF – 41/78 Occluded lumens – 9/78
rab11a	Recycling endosome GTPase	86%±18	60% (±7, 46, 18, p=0.0039)**	TEF – 23/46 Occluded lumens – 5/46
vangl2	Cell polarity, putative cargo	69%±18	34% (±14, 25, 3, p=0.0141)*	TEF – 7/25 Occluded lumens – 1/25
celsr1	Cell polarity, putative cargo	80%±10	33% (±4, 20, 3, p=0.0008)***	TEF - 6/20 Occluded lumens – 1/20
slc45a2 (control)	Pigmentation	82%±14.8	2% (±3, 26, 3)	-

Table S1.

^Genes reported in Zhong et al., HGG Advances 2022 (n=10)
***New genes reported in this study* (n=15)**
TEF – trachea-esophageal fistula
SEM – standard error of the mean, n=number of embryos assayed, N=number of independent experiments p value determined by unpaired Student's t-test compared to *tyr* controls. $p<0.05$ indicates a significant frequency of TEF over controls.